IEEE Access
Multidisciplinary | Rapid Review | Open Access Journal

Received October 8, 2017, accepted November 4, 2017, date of publication December 6, 2017,
date of current version February 28, 2018.

Digital Object Identifier 10.1109/ACCESS.2017.2780277

The Art of Reading Explosion Phenomena: Science and Algorithms

SUMAYA ABUSALEH, (Member, IEEE), AUSIF MAHMOOD, (Senior Member, IEEE), AND KHALED M. ELLEITHY, (Senior Member, IEEE)
Department of Computer Science and Engineering, University of Bridgeport, Bridgeport, CT 06604, USA
Corresponding author: Sumaya Abusaleh (sumaya11abusaleh@gmail.com)

ABSTRACT Explosion phenomena today are considered a significant concern that needs to be detected and analyzed with a prompt response. We develop a multiclass categorization system for explosion phenomena using color images. Consequently, we describe four patterns of explosion phenomena, including pyroclastic density currents, lava fountains, lava and tephra fallout, and nuclear explosions, against three patterns of non-explosion phenomena, including wildfires, fireworks, and sky clouds. The classification task was handled through extracting different types of features, including texture features, amplitude features, frequency features, and histogram features. Then, these features were fed into several multiclass classification methods. In addition, we present a new data set for volcanic and nuclear explosions that includes 10 654 samples. Evaluation results show the one-against-one multiclass support vector machine with degree 3 polynomial kernel outperforms other classification methods. It produces the highest classification rate of 90.85% to categorize 5327 images of the data set. A reasonable execution time of approximately 117 ms was accomplished to classify one input test image.

INDEX TERMS Explosions, frequency-domain image analysis, image classification, image color analysis, image histogram analysis, image texture analysis, nuclear explosions, support vector machines, volcanoes.

I. INTRODUCTION

The explosion term was defined in our earlier work as "a rapid increase in volume, and a release of kinetic energy or potential energy. Kinetic energy includes radiant, electrical, or thermal energy, while potential energy includes nuclear or chemical energy. The explosion generates a blast pressure wave or shock wave, high temperature, and release of gases, in conjunction with loud and sharp sounds caused by the incidents that are associated with the occurrence of each explosion phenomena" [1].

An explosion can be a natural disaster such as a volcanic eruption. In contrast, it can be a critical man-made disaster such as a nuclear explosion. Volcanic eruptions can be classified based on the eruptive style. Thus, the eruption can have an explosive style when produces Pyroclastic Density Currents (PDCs) that are typically the most deadly and dangerous of all volcanic phenomena. However, the eruption can have an effusive style when generates lava fountains and flows that steadily ejected from the volcano onto the ground. In some cases, the lava and tephra fallout are emitted directly from a volcano during an effusive or explosive volcanic eruption [1]–[7].

On the other hand, based on the shape characteristic of a nuclear explosion, two major patterns can be formed in the explosion scene. Accordingly, a mushroom-shaped cloud is typically formed by the following types of nuclear explosions: atmospheric, surface, deep underground, and shallow underwater. Conversely, the space (high-altitude) explosion forms an artificial aurora view associated with an ionized region [1], [8].

Consequently, various systems are installed by U.S. Geological Survey (USGS) organization for monitoring volcanic eruptions [9]. However, they have limitations in temperature measurements, detection of ash clouds, detection of ground deformation, and transmission time of satellite systems. For example, the thermocouple probe that is used for measuring the lava temperature cannot be applied to difficult volcano locations. Since volcanologist can only perform the direct temperature measurements within the vicinity of a volcano, safe conditions must exist. Temperature measurements can also be made from a distance with cameras that measure thermal infrared radiation (TIR). However, TIR cameras can be completely or partially obscured by volcanic thick clouds (PDCs). Moreover, existing infrared satellite sensors

2169-3536 © 2017 IEEE. Translations and content mining are permitted for academic research only.
Personal use is also permitted, but republication/redistribution requires IEEE permission.
See http://www.ieee.org/publications_standards/publications/rights/index.html for more information.

capture only lava images of large areas with low resolution that limit the retrieval of fine-scale details from the volcanic thermal features [10].

Another limitation occurs when ground-based microwave radar systems are employed to measure volcanic fine ash. The fine ash becomes invisible to the radar system for distances greater than 50 km. Hence, the radio waves will not be reflected towards Earth, and might not be detected [11]. Conversely, ash cloud height and depth can be measured through observations generated from ground-based Light Detection and Ranging (LiDAR) optical systems. LiDAR systems typically demonstrate a higher sensitivity to the content of ash clouds as compared to microwave instruments, but counterbalanced by stronger path attenuation effects. Moreover, data collection and processing performed by LiDAR systems can be time consuming. LiDAR equipment is also expensive [12].

The GPS is deployed to monitor the ground deformation of a volcano. However, the operational utility of the Global Positioning System (GPS) is limited because it provides a small spatial and temporal coverage [13]. Furthermore, the limitation of the Moderate Resolution Imaging Spectroradiometer (MODIS) satellite remote sensing instrument is that MODIS retrieves ash clouds images within a lengthy time frame of fifteen to thirty minutes [14].

With regard to the limitations of nuclear detection systems that are deployed in the atmosphere and space, there are several contextual problems and difficulties related to the grid pattern of the system, the geography, and the site location [15].

Accordingly, acoustic systems can be affected by some natural phenomena such as volcanic eruptions, tornado, aurora, meteor, earthquake, wind patterns, and noise background. Moreover, debris sampling methodology can be impacted by previous tests, and patterns of the wind. Furthermore, electromagnetic pulse (EMP) can be affected by atmospheric lightning. In addition, satellites that use instruments to measure radiation from a nuclear detonation include: neutrons, gamma-rays, and x-ray are influenced by cosmic ray showers, solar radiation, and trapped particles. Additionally, atmospheric fluorescence is influenced by lightning and cloud cover. In contrast, radio techniques that include very low frequency (VLF), low frequency (LF), high frequency (HF), radio sounders, and Riometer are mainly affected by ionospheric disturbances, polar zone, auroral regions, and the creation of a proper grid pattern in some locations. Additionally, the local noise affects HF, radio sounders, and Riometer among other radio techniques. Another technique, referred to as magnetic-telluric, can be influenced by ionospheric disturbances, auroral disturbance, and magnetic disturbance. Lastly, debris resonance is impacted by previous tests, natural dust, and wind patterns that form at a high altitude that results in unpredictable grid pattern [15].

Because of the limitations of the current surveillance techniques for explosion phenomena, the need arises for maintaining the progress of developing new technical solutions that can perform a collaborative effort with the existing monitoring systems to identify imminent explosion hazards. In this context, the motivation behind designing the proposed classification system are fourfold. (1) Encounters diminishing of the explosion phenomena, (2) mitigation of the explosions' effect to save lives and properties when the classification system is linked to reliable automatic early warning systems and effective evacuation procedures, (3) defining physical properties of explosions that can be measured using color images, and (4) designing a technical solution that can detect and categorize explosion phenomena in a timely manner.

The remainder of the paper is organized as follows. Section II describes the problem background that includes different physical properties of the defined explosion patterns and explosion properties from image processing point of view. Section III illustrates several existing vision-based techniques that were applied to monitor explosion phenomena. Section IV highlights the research hypothesis and contributions. Section V explains the research methodology in the field of pattern recognition including feature extraction approaches and classification techniques. Section VI provides detailed description of a new dataset of color images that were used for conducting experiments. Section VII presents experimental results and discussion. Section VIII outlines prospects for the future. Section IX concludes this research.

II. PROBLEM BACKGROUND

In this section, we present the science behind the volcanic eruptions (natural explosions) and nuclear explosions (man-made explosions) in terms of how they normally occur. Consequently, we describe different physical properties of these phenomena that, in turn, have led to interpret the patterns of color images from image processing point of view.

A. VOLCANIC ERUPTIONS

The volcano is considered a natural way where the Earth has to release interior heat and pressure, which in turn causes rocks to melt and produce magma that is allowed to escape from the magma chamber through a vent in the Earth's crust. This force drives the eruption of a volcano. Moreover, two main factors typically dominate the violence of the eruption of a volcano. First, silica content. The more silica content of a magma, the more viscous or stickier it is, and the more explosive the produced eruption will be. Second, gas content. As the gas content increased, the eruption of the volcano will be more violent, and vice versa [1], [2].

Based on the eruptive style of the volcano and materials ejected during the eruption, three patterns of a volcanic eruption scene can be defined. (1) Patterns of the pyroclastic density currents, (2) patterns of lava fountains, and (3) patterns of the lava and tephra fallout. Consequently, the description of each phenomenon is given as follows:

1) PATTERNS OF PYROCLASTIC DENSITY CURRENTS

Pyroclastic Density Currents (PDCs) phenomena are usually the most destructive and deadly of all types of volcanic phenomena [16]. PDCs are mixtures of hot gases associated with pyroclastic materials that flow over the ground under the effect of gravity. The PDC phenomenon may generate from different mechanisms [1], [17]–[21]. For example, gravitational collapse of domes (Fig. 1a) [22], partial column collapse (Fig. 1b) [23], dome explosions (Fig. 1c) [24], overpressure at the vent (Fig. 1d) [25], steam-driven eruption column (Fig. 1e) [26], lateral blast (Fig. 1f) [27], boiling-over (Fig. 1g) [28], and continuous column collapse (Fig. 1h) [28].

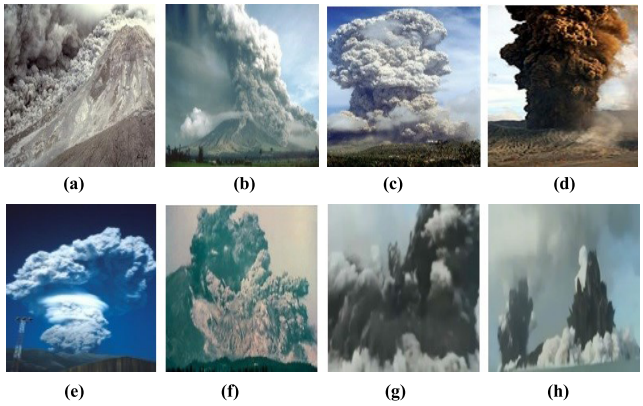

FIGURE 1. (a) The volcanic eruption of Soufriere Hills in Montserrat occurred on January 16, 1997 (photo credit: Richard Heard, Montserrat Volcano Observatory) [22]; (b) Mayon volcano occurred on September 23, 1984 (photo credit: Nicolas Lardot, Wikimedia Commons website) [23]; (c) Soufriere Hills volcano, Montserrat (photo credit: Barry Voight, National Science Foundation website - date of the image is unknown) [24]; (d) Bromo volcano, East Java, Indonesia, occurred on 8 June, 2004 (photo credit: D. Wijayanto, Tom Pfeiffer/ Volcano Discovery website) [25]; (e) The eruption of Guagua Pichincha volcano, west of the capital Quito, Ecuador occurred on October 7, 1999 (photo credit: U.S. Geological Survey, Department of the Interior) [26]; (f) Mount Saint Helens volcano, Washington State, USA, occurred on May 18, 1980 [27] (photo credit: U.S. Geological Survey, Department of the Interior); (g) The Tonga undersea volcanic eruption occurred on March 18, 2009 (photo credit: YouTube website) [28]; (h) The photo description and credit as per Fig. 1g [28].

Furthermore, the PDC phenomenon can be either a short-lived or relatively long-lived. The short-lived PDC is considered highly unsteady phenomenon, whereas the relatively long-lived PDC is considered sustained unsteady to quasi-steady phenomenon. The duration of both the transient current (short-lived) and sustained current (long-lived) rely on the volumetric flow rate as well as the total flow volume, influencing the behavior of the PDCs phenomena [19]. Fig. 1a-f represent mechanisms of short-lived PDCs. In contrast, Fig.1g, and Fig. 1h represent mechanisms of long-lived PDCs.

From image processing point of view, PDC patterns have non-luminous dense cloud shapes, numerous manifestation including avalanches, vertical column, laterally spread, and, natural mushroom plume, and the clouds color that can be white, gray to black shades, or brownish [1].

2) PATTERNS OF LAVA FOUNTAINS

Effusive eruptions such as shield volcanoes and fissure volcanoes produce lava that is magma rises towards the surface of the Earth, and flows out of the volcano as a viscous liquid. Typically, lava fountains and flows are varied and have multiple physical properties including [29]: (1) thickness, (2) length, (3) shape, and (4) width that depends on the following factors: lava type that is being erupted, discharge, slope of the ground where the lava travels, and the eruption duration. For example, Fig. 2a shows Kamoamoa eruption in Kilauea, Hawaii, on March 5, 2011 [30], and Fig. 2b displays the Kilauea's East Rift Zone (Pu'u 'Ō'ō) eruption on September 1983 [31].

FIGURE 2. (a) Fissure volcano -Kamoamoa eruption, Kilauea, Hawaii, on March 5, 2011 [30] (photo credit: U.S. Geological Survey, Department of the Interior); (b) The outpouring of lava fountains from the active shield volcano of Kilauea's East Rift Zone (Pu'u 'Ō'ō) on September 1983 (photo credit: U.S. Geological Survey, Department of the Interior) [31].

Lava fountains patterns have two properties from image processing point of view. First, a luminous glowing region. Second, the color of the lava during the eruption [1]. Accordingly, the color of the lava is based on its temperature. For example, it is stated in [32] that lava may glow white at approximately 1150 °C, golden yellow when its temperature nearly 1090 °C, orange at about 900 °C, bright cherry red at almost 700 °C, dull red when its temperature around 600 °C, or has the lowest visible red color at approximately 475 °C. As a matter of fact, the hotter the object, the brighter the light emitted will be. This process is called incandescence where the heat energy is turning into light energy.

3) PATTERNS OF THE LAVA AND TEPHRA FALLOUT

During an explosive or effusive eruption, a pattern can be formed when both the lava and tephra fallout are emitted directly from a volcano [1]. Tephra can be defined as a generic phrase for the accumulation of any airborne pyroclastic materials, for instance, fine ash, coarse ash, lapilli (cinders), Pele's hair, Pele's tears, blocks, bombs, and others. These materials are different in terms of type, size, shape, and condition when ejected from a volcanic vent [3]. Furthermore, Fig. 3a demonstrates lava and tephra fallout generated from the explosive eruption of Eyjafjallajökull in the island of Iceland that occurred on April 14, 2010 [33], and Fig. 3b illustrates the effusive eruption (basaltic volcanism) of Mt. Etna, Sicily, Italy that occurred in November 2002 [34].

From image processing point of view, lava and tephra patterns have the following properties. (1) A luminous

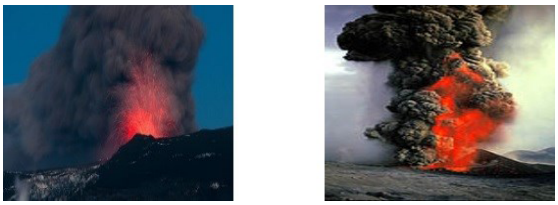

(a) (b)

FIGURE 3. (a) Explosive eruption of Eyjafjallajökull in the island of Iceland occurred on April 14, 2010 (photo credit: David Karnå, Wikimedia Commons website) [33]; (b) Effusive eruption (Basaltic volcanism) of Mt. Etna, Sicily, Italy, occurred in November 2002 (photo credit: Tom Pfeiffer / Volcano Discovery website) [34].

glowing region that represents the lava, (2) a non-luminous region that represents the tephra fallout, (3) the color of the lava that relates to its temperature, and (4) the color of the tephra that depends on the pyroclastic materials types that are being emitted during an explosive or effusive eruption [1]. For example, the tephra fallout can be either dark colored pyroclastic of basaltic to andesitic scoria or light colored pyroclastic of felsic pumice and ash [35].

B. NUCLEAR EXPLOSIONS

A nuclear explosion is defined as an explosion for which the energy is released by a nuclear transformation, either by fission or fusion [8]. Typically, nuclear explosions are classified based on the location of the point of burst in relation to ground zero [1]. Hence, nuclear explosions have the following five subcategories. (1) high altitude nuclear explosion (outer space detonation), (2) atmospheric nuclear explosion (air burst), (3) surface nuclear explosion, (4) deep underground nuclear explosion, and (5) shallow underwater nuclear explosion. In contrast, we propose to classify nuclear explosions based on the shape characteristic from image processing point of view. Thus, we define two patterns [1, 36]. (1) a mushroom-shaped cloud that is typically formed by the following types of nuclear explosions: atmospheric, surface, deep underground, and shallow underwater, and (2) an artificial aurora view associated with an ionized region that is formed by the space (high-altitude) explosion (e.g. Starfish space explosion [36]). This research will only focus through the experiments on identifying and classifying the nuclear explosions that form the mushroom-shaped cloud because of the lack of images of the high-altitude explosions. The description of the nuclear mushroom-shaped cloud is given below.

1) PATTERNS OF THE NUCLEAR MUSHROOM-SHAPED CLOUDS

The formation of the fireball and the rising mushroom cloud was described in [8] as follows. Typically, the nuclear explosion releases thermal energy. Most of the energy goes into heating of the bomb materials as well as of the air in the surrounding environment of the bomb. The temperature within the nuclear bomb itself reaches roughly tens of millions of degrees forming an intensely hot and luminous (gaseous) fireball. The fireball of a nuclear explosion can be viewed as flash or light from hundreds of miles away. Consequently, the diameter of the fireball keeps increasing to the maximum diameter in about 10s. Then, the fireball is no longer luminous, nevertheless it is very hot, and it behaves similar to a hot-air balloon, rising at a rapid rate.

The rising column of air creates a rising mushroom cloud which consists of hot gases in the stem, a toroidal circulation of hot gases inside the cloud head as the cloud reaches the upper atmosphere and begins to cool, in addition to vaporized fission products, weapon residues, debris from the surface of the Earth, and highly radioactive particles. The cloud keeps growing until it reaches its maximum height within about 4 minutes [8]. Fig. 4a, and Fig. 4b depicts the underground Buster Charlie nuclear explosion [36], and the Grable atmospheric nuclear explosion [36], respectively.

(a) (b)

FIGURE 4. (a) Buster Charlie underground nuclear explosion conducted on October 30, 1951 (photo credit: Gregory Walker, Trinity Atomic Web Site) [36]; (b) Grable atmospheric nuclear explosion conducted on May 25,1953 (photo credit as per Fig. 4a) [36].

In this context, the nuclear explosion can be defined from image processing viewpoint as follows. The mushroom-shaped cloud has a single orientation, the nuclear explosion has a luminous region while the fireball is forming for approximately 10s, a non-luminous region of the growing cloud that appears for 1-14 minutes after the fireball is no longer luminous, and the color of the mushroom cloud at which the initial color is naturally red/reddish, then it turns to white color because of the water condensation once the fireball cools [1], [8].

III. RELATED WORK

Several vision-based techniques were applied to monitor volcanic eruptions and nuclear explosions. In this view, Jinguuji and Ehara [37] proposed a remote sensing system by employing satellite images to compute the volcanic ash. This system is based on a physical model of volcanic ash motion. The model was tested on the Kuju volcanic eruption in Japan that occurred in 1995.

In the Lawrence Livermore National Laboratory [38], researchers presented the use of radar images taken from satellites that used the InSAR technique to monitor the Earth's surface from space. Researchers analyze these images to detect very small subsurface changes caused by underground nuclear explosions, and volcanic hazards. In addition, these researchers run simulations to characterize deformations.

Andò and Pecora [39] presented a new measurement tool that performed a real-time automatic thermographic analysis that used frames acquired by a thermal camera for volcanic activities of Mt. Etna and Stromboli in Italy. After the processing of a frame sequence, various information was provided that includes: the typology of the eruption, aspect, aspect ratio, maximum height, maximum width, and the duration of the analyzed sequence.

Langer *et al.* [40] classified volcanic tremor data at Mt. Etna in Italy based on supervised and unsupervised pattern classification techniques. Supervised classification was applied on an image dataset of four target categories namely: post-eruptive, eruptive, pre-eruptive, and lava fountain (effusive eruption). The totality of their dataset was 425 samples. Furthermore, the power feature was measured in frequency intervals, then a Multilayer Perceptron technique (MPL) and Support Vector Machine approach (SVM) were employed for classification. During the testing scheme, the output label was either '1' for the class, or '0' for all other classes. The SVM achieved an accuracy of 94.8%, and the MLP achieved an accuracy of 81.9%. On the other hand, unsupervised categorization was attained by employing self-organizing maps and cluster analysis approaches.

Iyer *et al.* [41] introduced a detection system for volcanic eruptions based on infrasonic signals. These signals contain information regarding the volcano's intensity that provides an approximation of ash column height. Consequently, unique cepstral-based features were extracted from the infrasonic signature of the volcano, and then fed to a Radial Basis Function Neural Network to distinguish eruptive activity among these three volcanoes including: Kasatochi located in Alaska, Tungurahua located in Ecuador, and Mt.St. Helens located in USA. Consequently, a total number of 25, 356 infrasonic data was obtained from the global infrasonic monitoring network dataset, and the waveform of each class was divided into 20 segments. Volcanic eruptions, based on the height of the ash column, were classified into the following classes: Strombolian, Vulcanian, Subplinian, and Plinian. As a result, a classification rate of 97% was achieved.

Also, Picchiani *et al.* [42] employed a single layer neural network to classify ash, or non-ash, and to retrieve the ash mass. Moreover, five datasets of MODIS images in the TIR spectral range were gathered in the 2001, 2002, and 2006 from the Mt. Etna volcanic eruptions. Each dataset includes 810, 000 samples. The architecture of the neural network included: the input space of three MODIS channels: CH28, CH31, and CH32, as well as a single hidden layer, and a single output layer. Results showed that approximately 90% accuracy was achieved.

Abusaleh *et al.* [1] introduced a novel classification system for some of explosion and non-explosion phenomena using color images. Explosion patterns include: lava fountains, lava and tephra fallout, pyroclastic density currents, and nuclear explosions. Whereas, non-explosion patterns include: fireworks, wildfires, and sky clouds. Three types of features were measured namely: texture features, amplitude features, and frequency features. Subsequently, the PCA algorithm was performed on each feature class to reduce the dimensionality of each feature vector to 100. Thus, the computed 300 features were fed into a multiclass SVM with degree 3 polynomial kernel. Moreover, the training dataset consist of 5, 327 samples, and the test dataset consist of 980 frames of YouTube video sequences, where each class comprises 140 frames for evaluation. As a result, about 94.08% accuracy was obtained to categorize the test set of 980 frames, and a processing time of 0.12s was consumed to classify one frame.

IV. RESEARCH HYPOTHESIS AND CONTRIBUTIONS

This research presents state-of-the-art explosion categorization through pattern recognition techniques on color images including feature extraction approaches and classification techniques. Consequently, color images are taken within the visible light spectrum range of approximately 400-700nm wavelength. These processed color images are 2-dimensional arrays of pixels with each pixel having RGB components.

The aims of employing multiple feature extraction approaches and several classification techniques in the proposed framework are twofold. First, calculate features that have the most relevant information to describe explosion phenomena from the input image data, which will result in reducing the computational cost. This factor is typically the challenge to perform the anticipated classification task of any application. Second, apply multiple classification techniques in order to categorize those phenomena and evaluate the performance of the developed system.

Furthermore, we develop a reliable framework that has multiple key properties: (1) each class is characterized by diverse feature sets. Since the computed features are invariant in terms of scale, rotation, illumination, and translation, they are considered highly discriminative, (2) the classification task is handled by various types of analysis including: texture, spatial, frequency, and histogram, (3) the research methodology provides various interpretations or views for a particular scene, and (4) accumulating these features in a single input vector will produce a meaningful and powerful insight into the images of the target application.

In this context, contributions of this research are as follows.

- We collect a new dataset of color still images called VNEX that stands for Volcanic and Nuclear Explosions, and it includes 10, 654 samples. Moreover, VNEX dataset includes four patterns of explosion phenomena: pyroclastic density currents, lava fountains, lava and tephra fallout, and nuclear explosions, against three patterns of non-explosion phenomena: wildfires, fireworks, and sky clouds. In view of that, using a large training set, a better approximation of the features that define the patterns are obtained. Hence, the classifiers will have a high generalization capability to perform precisely on new samples. Moreover, using a large testing set will result in getting a high confidence in the anticipated error rate. In fact, the error rate of any supervised classification system is anticipated by all obtainable

images that are usually divided into training and testing sets.

- We describe each image using multiple feature extraction approaches including: texture features by utilizing intensity levels, amplitude features by applying YCbCr color model, frequency features by exploiting Radix-2 Fast Fourier Transform (Radix-2 FFT) algorithm, and histogram features by employing Uniform Local Binary Patterns (ULBP) technique. The Principal Component Analysis (PCA) technique is then applied on each feature class to calculate the most significant 100 eigenvectors and the corresponding eigenvalues. Furthermore, these discriminative features are collectively encapsulated into a single vector of 400 length.
- We evaluate the effectiveness of the proposed features extraction methodology on the target application domain, and provide a comparison between numerous multiclass classification techniques in terms of the classification rate. These methods are: Euclidean distance, correlation, k-nearest neighbors, the one-against-one approach for multiclass support vector machines with various kernels, and the multilayer perceptron model (MPL). Lastly, we calculate the execution time for testing an input image using our developed classification system.
- The proposed framework is an enhancement of the design of the supervised classification system developed in [1]. Our proposed methodology as compared to [1] was evaluated on VNEX testing set of 5, 327 samples that differs from the testing set of 980 video frames used in [1]. Moreover, the proposed framework involves extracting 400 features (texture, color, frequency, and histogram) as compared to extracting 300 features (texture, color, and frequency) in [1]. As a result, a significant increase in the classification rate was accomplished using our research methodology. Furthermore, the proposed technical solution categorizes an explosion image in a timely manner as compared to MODIS satellite remote sensing instrument.

V. RESEARCH METHODOLOGY

A. FEATURE EXTRACTION APPROACHES

1) TEXTURE FEATURES

These features are computed by employing the PCA technique on pixel intensity values of the images. PCA is a statistical procedure that projects the high-dimensional data into a new lower dimensional space. The PCA aims to define the vectors that best account for explosion samples distribution within the entire eigenspace. Consequently, we resize the color images to 64×64 pixels during the preprocessing stage. Then, each sample (I_i) is converted to 8-bit grayscale vector (Γ_i). The PCA algorithm during training is performed in the following manner:

1) Find the Average Vector.

$$\bar{S} = (S_1 + S_2 + \cdots S_N)/N \tag{1}$$

where N = 5, 327, and dimensions of $\bar{S}$ is (4096 × 1).

2) For every image vector *i*, the mean adjusted vector is computed as:

$$\bar{S}_i = (S_i - \bar{S}) \tag{2}$$

Each mean adjusted vector is then assembled to form the mean adjusted matrix:

$$S_{mean} = [\bar{S}_1 \cdots \bar{S}_N] \tag{3}$$

In our application, S_{mean} dimensions will be (4096 × 5327).

3) Compute the covariance matrix.

$$C = \begin{bmatrix} Cov_{0,0} & Cov_{0,1} \cdots & Cov_{0,n} \\ \vdots & \cdots\cdots & \vdots \\ Cov_{n,0} & \cdots\cdots & Cov_{n,n} \end{bmatrix} \tag{4}$$

where $Cov_{i,j} = (S_i - \bar{S}) \cdot (S_j - \bar{S})$ that indicates matrix dot product, $\bar{S}$ = the average vector computed in step 1, S_i = the ith image vector, S_j = the jth image vector, and dimensions of C is (5327×5327).

4) Compute the eigenvectors and the corresponding eigenvalues of the covariance matrix. Thus, eigenvalues (λ) associated with C is solved using the following equation:

$$\det(\lambda I - C) = 0 \tag{5}$$

where det = the determinant of the matrix, and I = the identity matrix. Subsequently, for a given eigenvalue λ_K, the eigenvector V_K can be computed as follows:

$$(\lambda_k I - C) \times V_K \tag{6}$$

where V_K has dimensions of (5327×1). After sorting the 5, 327 eigenvalues that are computed by magnitude, we will keep the highest (100) eigenvalues, and the rest will be discarded.

5) Compute the basis vectors.
The 100 eigenvectors computed in step 4 will be accumulated into an eigenvector matrix:

$$EV_{matrix} = [EV_0 \cdots EV_{99}] \tag{7}$$

where dimensions of EV_{matrix} will be (5327×100). In order to compute the basis vectors, we multiply the mean adjusted matrix (S_{mean}) computed in step 2 by the EV_{matrix}:

$$S_B = S_{mean} \times EV_{matrix} \tag{8}$$

where S_B = the basis vectors which have dimensions of (4096 × 100).

6) Define each image by using a linear combination of the computed basis vectors. This representation is computed using the following formula:

$$Se = (S_{sample} - \bar{S})^T \times S_B \tag{9}$$

where S_{sample} = the sample with dimensions (4096×1), $\bar{S}$ = the average vector computed in step 1, and

S_B = the basis vectors computed in step 5. As a result, Se is the sample in the eigenspace that is represented by (100) numbers.

Each of the training dataset and the testing dataset contains 5, 327 samples. Hence, after applying the PCA to compute the most significant 100 eigenvectors and the corresponding eigenvalues, dimensions of the 2D training and 2D testing matrices are (5327×100).

2) AMPLITUDE (SPECTRAL) FEATURES

These features describe objects that refer to the physical domain from which they were created. Amplitude features in the proposed framework are measured by converting RGB images to YCbCr color space. Consequently, YCbCr splits the luminance component (Y) from chrominance components Cr and Cb, which are the red-difference as well as the blue-difference chroma components, respectively.

The choice of YCbCr color model for the image representation depends on the target application and the effectiveness of the color transformation algorithm. Typically, YCbCr is used in the context of digital images such as JPEG images. Furthermore, computing YCbCr of an image is more efficient than RGB, because the human eye is more sensitive to change in brightness than change in color [1]. Benoit Payette stated in [43] that red, green, blue, and luma components are in the gamma corrected space. No gamma correction is applied to color difference components Cb and Cr. Accordingly, RGB color space can be described as an illumination dependent color model. Moreover, engineers found that 60% to 70% of luminance (brightness) is in the green component of RGB. In the chrominance part Cb and Cr, the brightness information is removed from the blue and red colors. To overcome this disadvantage of RGB, we employ YCbCr.

We resize images to 64×64 pixels during the preprocessing phase. For each image, R, G, and B color components are extracted and converted to YCbCr. The transformation of RGB color space into YCbCr color space is implemented based on the following ITU-R BT.601 recommendation [44]:

$$\begin{bmatrix} Y \\ C_b \\ C_r \end{bmatrix} = \begin{bmatrix} 16 \\ 128 \\ 128 \end{bmatrix} + \begin{bmatrix} 0.257 & 0.504 & 0.098 \\ -0.148 & -0.291 & 0.439 \\ 0.439 & -0.368 & -0.071 \end{bmatrix} \cdot \begin{bmatrix} R \\ G \\ B \end{bmatrix}, \tag{10}$$

where each component of YCbCr is represented by 8-bits. The range of R, G, B components is between 0 and 255, while Y range is between 16 and 235. Additionally, the range of Cb values as well as Cr values is between 16 and 240. Y has an excursion of 219 and an offset of +16, placing black at code 16 and white at code 235, whereas Cb and Cr have excursions of ±112 and offset of +128.

After applying YCbCr color model, both of 2D output training matrix and testing matrix have dimensions of (5327 × 12288). Then, PCA is applied to compute the most significant 100 eigenvectors and the corresponding eigenvalues. Accordingly, the dimensions of the 2D components matrix that is used for training are equal to (5327 × 100). Likewise, the dimensions of the components matrix that is used for testing are equal to (5327 × 100).

3) FREQUENCY FEATURES

Before extracting these features, a preprocessing step is required, which is twofold. First, resizing each input color image in the time domain to 64×64 pixels. Second, converting the image (I_i) to a grayscale vector (Γ_i) of 8-bit intensity values. Furthermore, the frequency spectrum of an image is represented in terms of the sum of sinusoidal waves using the Radix-2 Fast Fourier Transform (FFT) algorithm [45]. These waves are eignfunctions of linear, constant-coefficient, and differential equations. Hence, they preserve their identity in a linear system where they can change the amplitude and the phase of the sinusoids, however, cannot change their basis structure. As a result, it discloses information that is considered significant regarding the geometric structure of the 2-dimensional spatial image, and the speed of Radix-2 FFT comes at a cost of complexity at which the total computation is proportional to $N\log_2(N)$. The discrete formula of this algorithm is given below [1], [46]:

$$X_k = \sum_{m=0}^{N/2-1} x_{2m} e^{-\frac{2\pi i}{N}(2m)^k} + \sum_{m=0}^{N/2-1} x_{2m+1} e^{-\frac{2\pi i}{N}(2m+1)^k} \tag{11}$$

Typically, if the gray levels of the entire image are changing slowly, that implies the image contains low-frequency components. In contrast, if the gray levels of the image are changing rapidly, that implies the image contains high-frequency components [1]. Furthermore, the frequency-domain description provides an increasingly accurate characterization of the object in the image as more coefficients are calculated. As a matter of fact, the larger the input image in the spatial domain, the more data is sent for calculation, the better precision of Radix-2 FFT is achieved, and the less noise. In the implementation of our system, we first calculate the frequency components, then we employ PCA algorithm on the output complex vectors in order to focus on the dimensions such that a high variance between samples vectors exists. Consequently, input 2D training and testing matrices in the time domain, and complex output 2D training and testing matrices in the frequency domain are identical in terms of size. Each of which is of dimensions (5327 × 4096). After employing PCA on output matrices to compute the most significant 100 eigenvectors and the corresponding eigenvalues, the dimensions of both training and testing components matrices are (5327 × 100).

4) HISTOGRAM FEATURES

The Uniform Local Binary Patterns (ULBP) approach is employed to extract histogram features of the images of our application domain. ULBP is considered a local matching approach for pattern recognition, and it uses a set of local observations obtained from an explosion image to derive a model of a precise explosion pattern, which is subsequently used for classification. Indicating only uniform patterns of the

entire image contributes to dimensionality reduction of the features vector length, computational simplicity, and increasing the classifiers performance as the computed histogram features are invariant to image rotation, scaling, illumination, and translation.

Consequently, we resize each input color image to 92×112 pixels, and we convert it into 8-bit gray scale. Then, we divide the gray scale image into 5 × 5 blocks. The LBP operator creates labels for image pixels in each block through thresholding the eight neighborhoods with the center pixel value. The new value for the center pixel (x_c, y_c) is computed through concatenating all binary numbers in a clockwise direction. The value of the $LBP_{P,R}$ operator of (x_c, y_c) is defined as follows [47]:

$$LBP_{P,R}(x_c, y_c) = \sum_{P=0}^{P-1} f(i_p - i_c)\, 2^p \tag{12}$$

where the representation (P, R) denotes pixel neighborhoods at which P is the sampling points on a circle that has a radius R, and the symbols i_c and i_p are the values of the gray levels of the central pixel as well as the surrounding pixels. In our implementation P = 8, and R = 1. Additionally, the function f(h) is given as follows 47]:

$$f(h) = \left\{ \begin{array}{ll} 1, & \text{if } h \geq 0 \\ 0, & \text{if } h < 0 \end{array} \right\} \tag{13}$$

Fig. 5 illustrates the basic LBP operator such that the binary number 01111100 is equivalent to 124 decimal number. Therefore, (x_c, y_c) value will be modified to 124. This process is repeated by iterating over the entire block, and keeps updating each pixel value.

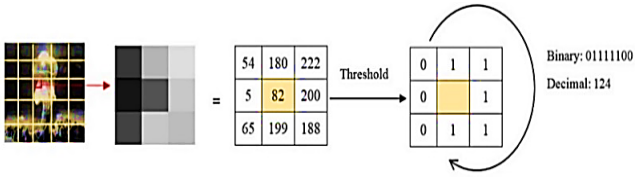

FIGURE 5. An illustration of the basic local binary pattern operator utilizing a nuclear explosion example.

Furthermore, we compute the uniform patterns for the entire image through the following procedure. We generate uniform patterns for each block if there are no more than two bitwise transitions from zero to one or vice versa once the binary bit pattern is circularly traversed. For instance, 00000001 (2 transactions) is a uniform pattern. Whereas, 01000001 (4 transactions) is a non-uniform pattern. As a result, the uniform patterns for the entire block will be within [0-57], and then we concatenate all regional histograms to construct a global description of the nuclear explosion image in our example. Hence, we represent each input image by (5 × 5 × 58) features. Fig. 6 depicts this procedure.

After representing 5, 327 samples of training and testing sets using ULBP algorithm, dimensions of the corresponding 2D matrices are (5327 × 1450). In fact, the background of any image will be preserved using ULBP because most of the pixels typically have the same gray level value within each background region of the same image. In order to overcome this drawback, we compute the most significant 100 eigenvectors and the corresponding eigenvalues using the PCA technique. Therefore, both 2D components matrix for training set as well as for testing set are of dimensions (5327 × 100).

B. CLASSIFICATION TECHNIQUES

The supervised learning task is performed in order to map the input data to the desired output data at which both data are labeled. Thus, the space will be separated into classes or regions. In this section, we discuss the following multiclass classification techniques that we employ in our experiments.

1) CONVENTIONAL STATISTICAL METHODS

Each example in the learning dataset is represented by a set of four vectors as follows: the first vector (at) consists of 100 texture features calculated using PCA algorithm on image intensity levels. The second vector (bt) comprises 100 amplitude features computed using YCbCr + PCA. The third vector (ct) contains 100 frequency features calculated using Radix-2 FFT + PCA, and, the fourth vector (dt) includes 100 histogram features measured using ULBP + PCA.

Subsequently, these vectors are combined in one input vector for the training phase called Training Combiner Vector ($TRCV_i$) that has length of 400. Equation 14 summarizes the combination step. Likewise, this procedure will be repeated for each sample (i) in the testing set. As a result, each unknown sample will be presented using a Testing Combiner Vector ($TTCV_i$) during the testing stage.

$$[TRCV_i]_{400\times 1} = \left[\begin{array}{l} [at_0, at_1, \cdots, at_{99}] + [bt_0, bt_1, \cdots, bt_{99}] \\ + [ct_0, ct_1, \cdots, ct_{99}] + [dt_0, dt_1, \cdots, dt_{99}] \end{array} \right]_{400\times 1} \tag{14}$$

Thus, we apply the following conventional statistical methods.

a: EUCLIDEAN DISTANCE (ED)

Image vectors are considered points in the feature space. Hence, for each image feature vector ($TTCV_i$) in the testing set, the Euclidean distance (ED) is measured with every image feature vector in the training set TRCV $(0, \cdots, n-1)$, where n = 5, 327. Consequently, the minimum distance is stored, and its corresponding label is calculated. Euclidean distance is defined as follows.

$$ED_{TRCV,TTCV} = \sqrt{\sum_{i=0}^{n-1} (TRCV_i - TTCV_i)^2} \tag{15}$$

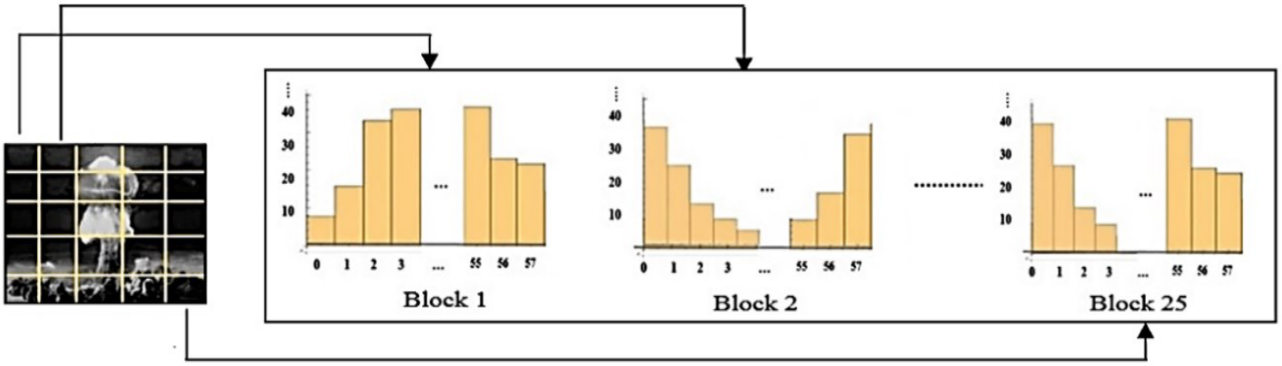

FIGURE 6. A uniform pattern histogram is extracted for each block in the entire image, and then all histograms are concatenated in a single histogram.

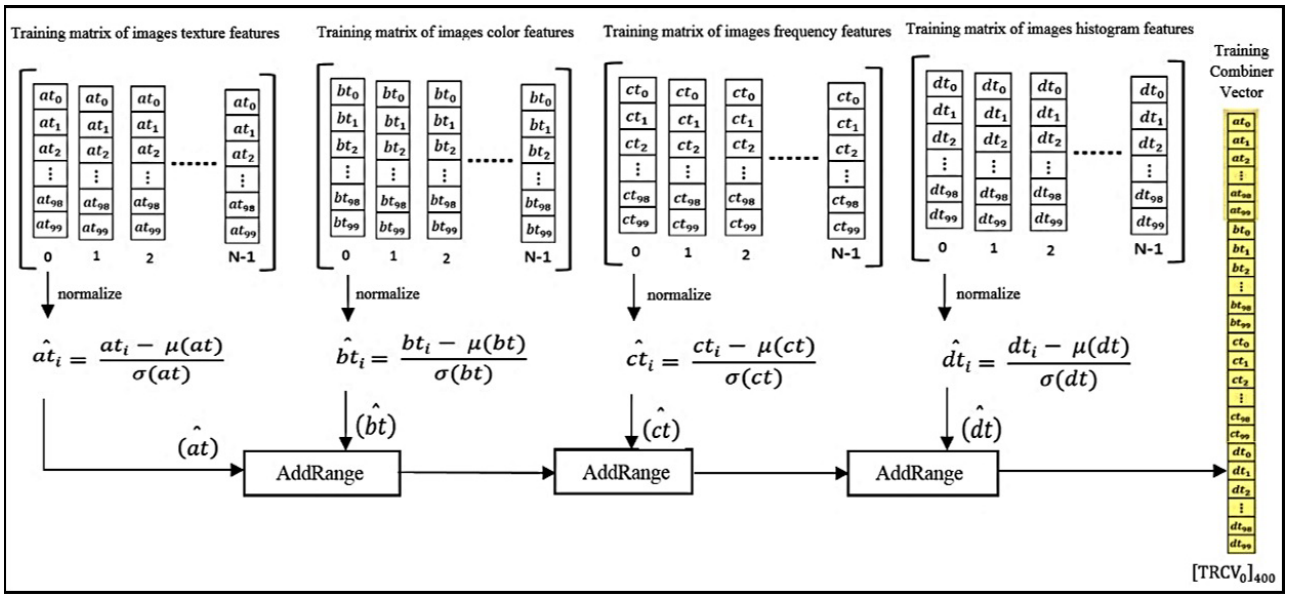

FIGURE 7. A graph for combining features that represents the first image in the training set.

b: CORRELATION(C)

The correlation indicates the strength and direction of the inner relationship between two image feature vectors in the feature space. Hence, for each image feature vector ($TTCV_i$) in the testing set, the correlation is measured with every image feature vector in the training set $TRCV(0, \cdots n-1)$, where $n = 5,327$. Then, the maximum correlation value is stored, and its corresponding label is calculated. Correlation is given as follows.

$$C_{TRCV,TTCV} = \frac{\sum_{i=0}^{n-1}\left(TRCV_i - \overline{TRCV}\right)\left(TTCV_i - \overline{TTCV}\right)}{\sqrt{\sum_{i=0}^{n-1}\left(TRCV_i - \overline{TRCV}\right)^2 \sum_{i=0}^{n-1}\left(TTCV_i - \overline{TTCV}\right)^2}} \tag{16}$$

2) CLASSIFIERS

The abovementioned feature vectors in the sequence {(at), (bt), (ct), and (dt)} for each sample of the training set were normalized to be within the interval $[-1,1]$. Hence, for each component of a particular features vector, we subtract the mean (μ), then divide by the standard deviation of that corresponding vector values (σ). Then, these four feature vectors were combined in one input vector of length 400 ($TRCV_i$). Therefore, equation (17) describes a modified version of equation (14) after applying the normalization function. Moreover, Fig. 7 depicts the combining procedure of the measured features of the first input image in the training set where the number of training samples (TS) is 5,327, and AddRange is a method in C# language that adds the elements of a normalized vector to the end of a list.

$$\begin{aligned}[TRCV_i]_{400\times 1} = {} & [\text{normalize}([at_0, at_1, \cdots, at_{99}]) \\ & + \text{normalize}([bt_0, bt_1, \cdots, bt_{99}]) \\ & + \text{normalize}([ct_0, ct_1, \cdots, ct_{99}]) \\ & + \text{normalize}([dt_0, dt_1, \cdots, dt_{99}])_{400\times 1}\end{aligned} \tag{17}$$

Similarly, normalization is employed to the computed feature vectors values for each sample of the testing set before being combined in one input vector ($TTCV_i$) of length 400. Consequently, we employ the following classifiers.

a: K-NEAREST NEIGHBORS (KNN)

It is a non-parametric approach for performing a supervised classification. It aims to determine a predefined value (K) of training samples (TS) closest in terms of distance to a new sample, and predict its label among TS. Thus, an unknown test sample is classified as it belongs to the category among its nearest neighbors that has the majority vote [48]. In our work, KNN is tested where $K = 1$, 3, or 5, $TS = 5,327$, the number of output classes $(M) = 7$, and $[TRCV_i]_{400\times1}$ is the corresponding input vector of each sample (i) of TS.

b: ONE-AGAINST-ONE APPROACH FOR THE MULTICLASS SUPPORT VECTOR MACHINE (SVM)

This technique concurrently decreases the empirical error of the categorization while finding the superlative separating hyperplane that maximizes the margin between the closest points of classes. The margin represents the distance from the hyperplane to the closest data points in the feature space.

Data points that are residing along the margin are called ''support vector points.'' Hence, a linear combination of only these data points represents the solution [49].

The effectiveness of the SVM classifier relies on selecting the appropriate kernel function $K(x_i, x_j)$. This step is considered the first and the most important step in applying SVM to real-world data sets, and it is usually declared as the ''kernel trick.'' Accordingly, we employ the most common kernels to map the data points of an input space to a high-dimensional feature space. Thus, exploring the kernel that leads to generate the highest classification rate. These kernels are [50]:

- Linear kernel, which is given as follows:

$$K(x_i, x_j) = x_i^T x_j \tag{18}$$

- Polynomial kernels of degree 2 ,3, 4, 5, and 6, which is given as follows:

$$K(x_i, x_j) = \left(\gamma x_i^T x_j + r\right)^d, \quad \gamma > 0 \tag{19}$$

- Gaussian kernel: Radial Basis Function (RBF), which is given as follows:

$$K(x_i, x_j) = \exp\left(-\gamma \left\|x_i - x_j\right\|^2\right), \quad \gamma > 0 \tag{20}$$

- Sigmoid function, which is given as follows:

$$K(x_i, x_j) = \tanh\left(\gamma x_i^T + r\right) \tag{21}$$

where d, γ, r are kernel parameters.

Typically, SVM is considered a binary classification technique. However, it is possible to enhance it in order to handle multinomial classification problem through constructing multiple machines. Thus, we employ one-against-one (abbreviated in this paper as 1-against-1) SVM approach to deal with the multiclass problem under consideration. During training process, this approach creates a machine for each pair of categories, producing $K = M(M-1)/2$ machines, where $M = 7$ target classes, $K = 21$ machines, and $TS = 5,327$, and $[TRCV_i]_{400\times1}$ is the corresponding input vector of each sample (i) of TS. Furthermore, the Sequential Minimal Optimization (SMO) algorithm is used because it can quickly solve the SVM optimization quadratic problem (QP) to discover the optimal combination of the hyperplane parameters by dividing the problem into lower dimensional sub-problems and solving it without significantly depending on a numerical optimization technique [51].

During the testing phase of the SVM classifier, a new unknown test sample (sa) is categorized as belonging to class l^* whose decision function (f_{l^*})generates the maximal value. The equation is provided as follows [1]:

$$l^* = \arg \max_{l=1,\ldots,M} f_l(sa) = \arg \max_{l=1,\ldots,M} \left(w_l^T \varphi(x) + b_l\right) \tag{22}$$

c: A MULTILAYER PERCEPTRON (MLP)

It is a non-linear neural network model that is useful for solving supervised learning problems. MPL approximates a classification function that maps the input vector $[TRCV_i]_{400\times1}$ into a particular class. The architecture of the MLP model used in our experiments comprises three layers of nodes as follows: (1) one input layer that is identical in terms of length to the $TRCV_i$ input vector, (2) hidden layers ranging from one to four, and (3) one output layer where the number of the output neurons is seven. Furthermore, the sigmoid activation function is employed, and the Mean Square Error (MSE) is used as a criterion of the classification accuracy of the target application.

While training this model, the backpropagation algorithm using Stochastic Gradient Descent (SGD) is employed. The objective of backpropagation training algorithm is to reduce the MSE between the correct target output and the actual output from perceptron. Backpropagation training algorithm operates in the following two main phases [52]:

- The network takes the training input vector $TRCV_i$ that will be allowed to pass forward through various layers in order to calculate the output for each node. Then, these outputs of the neuron nodes in the output layer are compared as opposed to their desired answers or responses to yield the error term.
- A backward pass via neural network during which the proper error signal propagates to each node, as well as the corresponding changes of weights are modified.

During the testing phase of MPL, each unknown input pattern is allowed to propagate through various layers, and it is typically classified as it belongs to the category of the output node that produces a high value, compared with lower values in all other nodes.

VI. DATASET

The evaluation of our proposed framework is performed on a new dataset of images that was collected by Sumaya

Abusaleh during 2014-2017. In this research, we will abbreviate our dataset as (VNEX) that stands for Volcanic and Nuclear Explosions. Furthermore, images of VNEX dataset were downloaded from different resources. For example, USGS website [53], Wikimedia Commons [54], Volcano Adventures website [55], Volcano Discovery website [56], National Oceanic and Atmospheric Administration (NOAA), National Weather Service website [57], Trinity Atomic website [36], PEXELS blog [58], and others.

VNEX dataset consists of 10, 654 color still images distributed among 7 classes including 4 classes for explosion phenomena patterns, against 3 classes for non-explosion phenomena patterns. Explosion phenomena classes include: (1) pyroclastic density currents (PDC), (2) lava fountains (LF), (3) lava and tephra fallout (LT), and (4) nuclear explosions (NC). On the other hand, non-explosion phenomena classes include: (1) wildfires (WF), (2) fireworks (F), and (3) sky clouds (SC).

Furthermore, the proposed categorization system works in two stages: training and testing. Tainting and testing images of VNEX are independent. Overall, there are 5, 327 training images and 5, 327 testing images. Table 1 illustrates the number of images in each class of training and testing sets.

TABLE 1. Dataset categories.

Category	Number of images		Total
	Training	Testing	
PDC	1522	1522	3044
LF	966	966	1932
LT	346	346	692
NC	394	394	788
WF	625	625	1250
F	980	980	1960
SC	494	494	988
Total	5327	5327	10654

Since VNEX categories are imbalanced distributions of images per each category, each class of VNEX dataset is divided into 50% images for training and 50% images for testing for consistency. Furthermore, while collecting the images of VNEX, we faced a difficulty on finding a large number of nuclear mushroom-shaped clouds (NC) images and the lava and tephra fallout (LT) images. Therefore, in the scenario where if the VNEX dataset was divided into 30 % for training and 70% for testing per each category, we will have about 913 of PDC samples for training, and 2131 of PDC samples for testing, and this division in this case can be considered sufficient for performing the desired classification task. In contrast, we will have about 236 of NC samples for training, and about 552 NC samples for testing. Similarly, we will have about 208 LT samples for training and about 484 LT samples for testing. Consequently, about 236 of NC training samples and 208 of LT training samples are relatively not enough to learn the classifiers under consideration. As a result, we have found through our experiments that the small number of samples for training will not be enough to learn the best hyperplane (decision surface) that can fit the training input vector properly, and hence have led to low accuracy using multiclass SVMs with different kernels, and MPL that uses the backpropagation training algorithm.

Furthermore, an explosion and non-explosion phenomenon may occur during the day or the night. Therefore, VNEX images have different backgrounds. In addition, we crop the area of an explosion or non-explosion of VNEX images manually, and then we save all samples using JPEG file format. Fig. 8 displays nine random examples from the respective seven classes.

Explosion patterns of VNEX dataset including PDC, LF, LT, and NC are described in section II. Therefore, we will provide in this section a description for the non-explosion patterns of VNEX dataset from image processing point of view. Consequently, wildfires patterns from image processing point of view contain a non-luminous region, a luminous region, or both. The luminous region that usually appears in the scene of a wildfire is related to the flame that is produced during the flaming phase of the combustion process, and its color variation depends on the type of the material being burned, how hot it's burning, and the amount of oxygen that is available to turn all the carbon into carbon dioxide (CO_2). The flame color of the wildfires typically glows red transmitting to orange, then to yellow. On the other hand, the non-luminous region of a wildfire scene is related to the smoke that is generated during the smoldering phase of the combustion process. This smoke tends to reflect the light making the smoke appears white. Likewise, tree trunks and big branches may have large amounts of moisture that are prone to smolder and emit steam that turns the smoke white. In addition, a black soot of fine particles is formed and released into the air during the hot burning of the dry underbrush. Thus, the smoke may appear black in a wildfire scene [1], [59].

Fireworks patterns from image processing point of view have the following properties. First, a black background because they are typically displayed in the night. Second, they have multiple ignitable shapes such as: glitter, spinner, tail, willow, brocade, stars, and others. Third, they have different colors that are related to the type of the metal salt which produces a light that travels at a specific wavelength [60]–[62].

Clouds patterns from image processing point of view have different shapes. For example, high-level clouds include Cirrus that have wispy and feathery shape, Cirrostratus have relatively transparent form of a widespread veil-like layer, and Cirrocumulus that are layered clouds performed with small cumuliform lumpiness, and have rippled shapes, whereas mid-level clouds include Altostratus that possess a flat and uniform type texture, Altocumulus that are heap-like clouds, and Nimbostratus that have dark, thick, and lumpy layer. Furthermore, low-level clouds include Stratus that are dull gray clouds that developed horizontally, and Cumu-

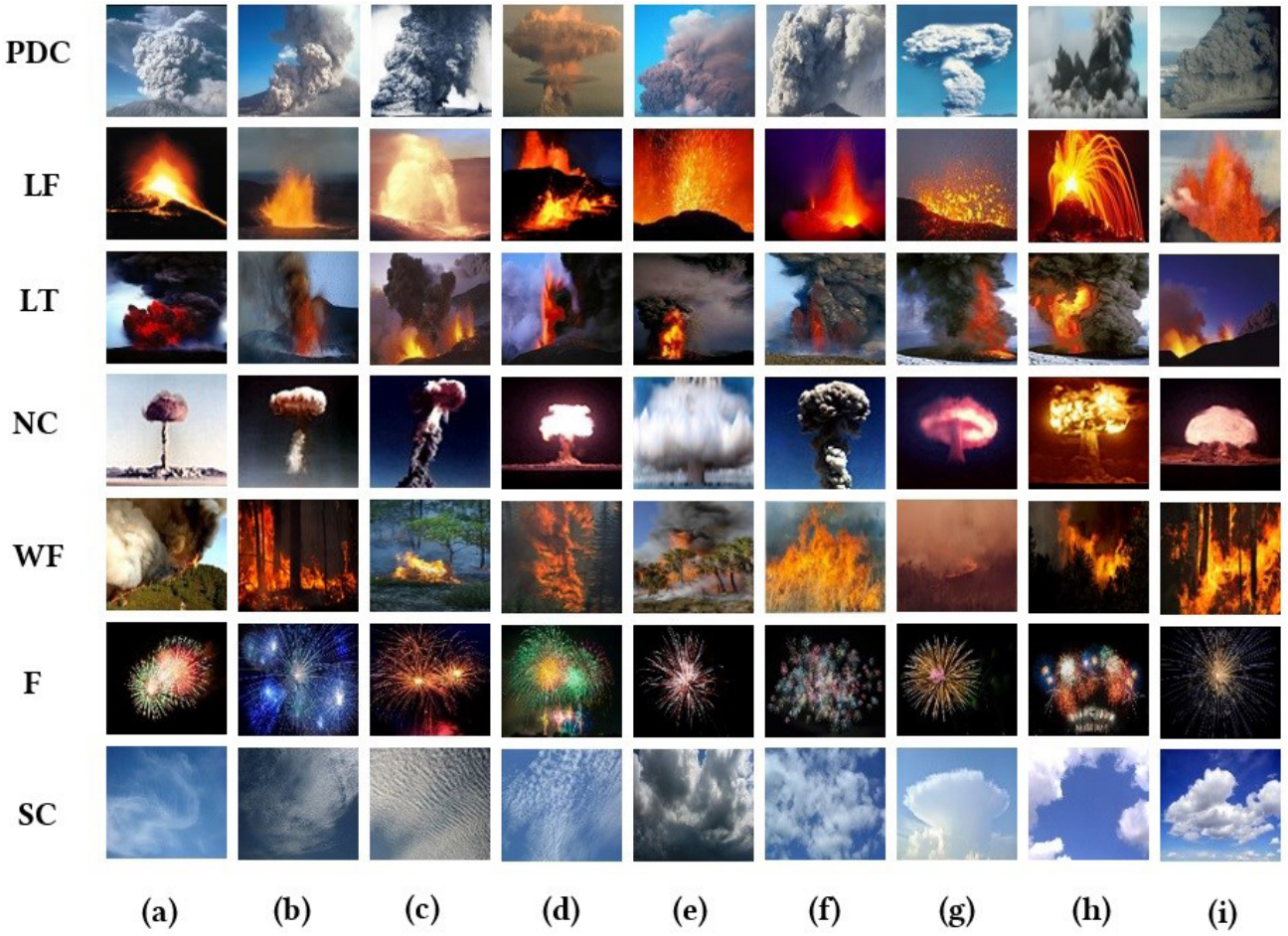

FIGURE 8. Random samples of VNEX dataset. PDC: a-d (photos credit: U.S. Geological Survey, Department of the Interior) [65]–[68], e (photo credit: Dr. Allan Sauter, SCRIPPS, and National Oceanic and Atmospheric Administration, U.S. Department of Commerce, U.S. Office of Ocean Exploration and Research.) [69], f (photo credit: Itu, Wikimedia Commons) [70], g (photo credit: Paginario, Wikimedia Commons) [71], h (photos credit: YouTube website) [28], and i (photo credit: R. Russell, Alaska Department of Fish and Game, U.S. Geological Survey) [72]; LF: a (photo credit: Jeffrey B. Judd, U.S. Geological Survey) [73], b and c (photos credit: U.S. Geological Survey, U.S. Department of the Interior) [74], d (photo credit: Nordic Volcanological Institute, Reykjavik, Iceland, Photographer: Gudmundur E. Sigvaldason, U.S. Geological Survey website) [75], and e-i (photos credit: Tom Pfeiffer / Volcano Discovery website) [76]–[79]; LT: a-i (photos credit: Tom Pfeiffer / Volcano Discovery website) [80]–[83]; NC: a-d, and f-i (photos credit: Gregory Walker, Trinity Atomic Web Site) [36], and e (photo credit: Nevada Field Office, National Nuclear Security Administration) [84]; WF: a (photo credit: John Newman, Wikimedia Commons website) [85], b (photo credit: Tatiana Bulyonkova, Wikimedia Commons website) [86], c (photo credit: Tilo, Wikimedia Commons website) [87], d (photo credit: Evil Saltine, Wikimedia Commons website) [88], e (photo credit: Ramos Keith, Wikimedia Commons website) [89], f (photo credit: U.S. Fish and Wildlife Service, Gerald Vicker, Wikimedia Commons website) [90], g (photo credit: Flip Schulke, U.S. National Archives and Records Administration, Wikimedia Commons website) [91], h (photo credit: US Air Force, Wikimedia Commons website) [92], and i (photo credit: Tatiana Bulyonkova, Wikimedia Commons website) [93]; F: a-i (photos credit: PEXELS blog website) [85]; SC: a-c, and e (photos credit: National Oceanic and Atmospheric Administration, Department of Commerce, National Weather Service) [64], d (photo credit: Simon Eugster, Wikimedia Commons website) [94], f (photo credit: Saperaud, Wikimedia Commons website) [95], g (photo credit: Simon Eugster, Wikimedia Commons website) [96], h (photo credit: Joniprittie, Wikimedia Commons website) [97], and i (photo credit: Michael Jastremski, Wikimedia Commons website) [98].

lus that are the stereotypical fluffy clouds that developed vertically, Stratocumulus that are small lumpy clouds, and Cumulonimbus that are tall and fluffy. In addition, color of the clouds is the second property. When all different colors of light hit a water droplet or ice crystal of the cloud that has an average size of about 10 micrometers. They scatter equally into colors of rainbow; then they combine to produce a white light. Hence, clouds typically appear white [63], [64].

VII. EXPERIMENTAL RESULTS AND DISCUSSION

We implemented the classification system using C Sharp programming language under the Microsoft .Net framework 4.6, and it operates on a workstation that has an Intel(R) Core(TM) i7 CPU @ 3.20 GHz with 20.0 GB RAM, and 64-bit operating system. Experiments are divided into two main scenarios as follows.

A. SCENARIO I

Comparing our approach with the approach proposed in [1], the same setup was followed in carrying out the experiments. Primarily, number of classes is 7 namely: "PDC, LF, LT, NC, WF, F, and SC," and we use the same training set of 5, 327 images for learning the multiclass SVM with degree 3 polynomial kernel. In addition, we use the same video sequences

of a total 140 frames per each class for testing the classifier. However, the difference lies in the number of extracted features. Thus, each image is defined using an input vector of length 400 exploiting texture, color, frequency, and histogram features in our approach, as compared to an input vector of 300 length exploiting texture, color, frequency features to represent each image in [1]. Subsequently, we compute the accuracy of the classification system using the following formula:

$$\text{Accuracy} = \frac{\text{TP} + \text{TN}}{\text{FN} + \text{FP} + \text{TN} + \text{TP}} \times 100\% \qquad (23)$$

where *FN*, *FP*, *TN*, *and TP* are the number of false negative, false positive, true negative, and true positive cases, respectively.

As a result, by employing the proposed methodology in this research, we achieved a significant increase of 4.08% in the average accuracy from 94.08% to 98.16% because of the approximate increase of 1.43 % in PDC precision, 9.29% in LF precision, 8.57% in LT precision, and 9.29 % in WF precision. Fig. 9 illustrates the comparison between both approaches in terms of the accuracy (classification rate) for the seven classes under consideration.

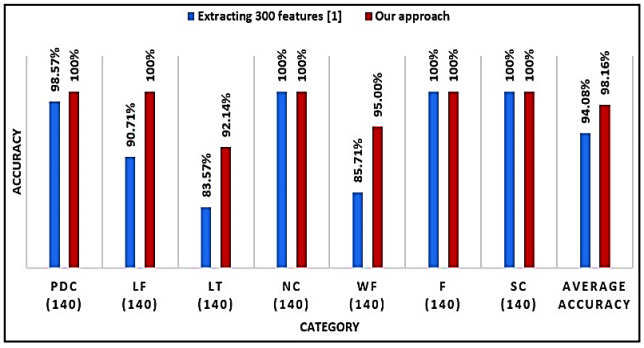

FIGURE 9. Comparison between our proposed methodology and the classification system proposed in [1] in terms of accuracy.

B. SCENARIO II

Extensive experiments were conducted to determine the classification model that can achieve the best performance in terms of classification rate of testing instances of VNEX dataset. Thus, the 1-against-1 multiclass SVM with degree 3 polynomial kernel has a superior classification rate in comparison to other classification methods being applied. It generates the highest accuracy of 79.16% and 90.85% when extracting 300 features (texture, color, and frequency) and 400 features (texture, color, frequency, and histogram), respectively. In addition, results inclusively show that extracting 400 features performs consistently better when utilizing all multiclass classification techniques under consideration including: Euclidean distance, correlation, KNN, SVM, and MPL, rather than the research methodology of extracting 300 input features [1] with the increase in the number of new testing samples. Table 2 demonstrates a performance comparison between different multiclass classification methods

TABLE 2. Performance Comparison of multiclass classification methods when extracting 300 features against 400 features of vnex testing set (5, 327).

Category		Accuracy (input vector of 300 features)	Accuracy (input vector of 400 features)
ED		77.23%	77.42%
C		77.81%	78.02%
KNN	K value =1	77.25%	77.42%
	K value =3	76.42%	76.70%
	K value =5	76.00%	76.22%
SVM	Linear	73.21 %	85.24%
	Polynomial 2	75.60 %	86.77%
	Polynomial 3	**79.16 %**	**90.85%**
	Polynomial 4	70.87 %	83.54%
	Polynomial 5	24.82 %	28.57%
	Polynomial 6	24.82 %	28.57%
	RBF	32.38%	35.09 %
	Sigmoid	71.92 %	81.72%
MPL		72.24%	82.05%

under consideration in terms of accuracy when extracting 300 features as opposed to 400 features of VNEX testing dataset.

Devoting to analyzing the behaviors of the multiclass classification systems that we addressed, conventional statistical methods including Euclidean distance (ED) and correlation (C) are not suitable to classify samples of VNEX dataset, because they are complex and in a large-scale space. Hence, giving a preference to predict the output label based on the minimum distance or maximum correlation has produced a poor performance of 77.42% and 78.02% using Euclidean distance and correlation, respectively.

Although KNN demonstrates a short time interval for the training phase, it has two drawbacks as follows: (1) each neighbor is equally important, and (2) the imbalanced training data is more likely to affect the performance of KNN. Thus, classes that have a large number of samples typically have a higher possibility to win. Intuitively, that explains why the KNN accomplished a poor classification rate of 77.42%, 76.70%, 76.22% when the value of k was set to 1, 3, and 5, respectively.

Furthermore, the kernel takes relationships in the data that are normally implicit and makes them explicit. As a result, the patterns classification takes place more easily. This is the reason behind the success of the kernel-based approaches such as SVM [99]. In this context, our results show the impact of selecting the proper kernel as a critical step when employing 1-against-1 multiclass SVM approach. Accordingly, the polynomial kernel of degree 3 has led the SVM classifier to produce the highest classification rate of 90.85% for testing VNEX samples of 400 input features vector. Hence, it outperforms the SVM with a linear kernel, the SVM with a RBF kernel, and the SVM with a sigmoid kernel that produced a classification rate of 85.24%, 35.09 %, and 81.72%, respectively. Also, the empirical classification error using SVM increases as higher degree polynomials kernels are employed, which in turn tend to cause overfitting in the training set.

Thus, polynomials 4, 5, and 6, generated a classification rate of 83.54%, 28.57%, and 28.57%, respectively.

Consequently, Table 3 presents a comparison between various multiclass classification techniques in terms of classified against misclassified images of VNEX testing set of a total 5, 327. The system evaluated two cases as follows. First, when texture, color, and frequency features were collectively accumulated in one input features vector of 300 length, as per the methodology proposed in [1]. Secondly, when texture, color, frequency, and histogram features in the current enhanced solution, are accumulated in one input vector of 400 length for each sample.

TABLE 3. Classified against misclassified images of VNEX testing set (5, 327) when the input vector length = 300, as compared to the Input vector of length 400.

Category		Input vector = 300		Input vector = 400	
		Classified	Misclassified	Classified	Misclassified
ED		4114	1213	4124	1203
C		4145	1182	4156	1171
KNN	K value =1	4115	1212	4124	1203
	K value =3	4071	1256	4086	1241
	K value =5	4049	1278	4060	1267
SVM	Linear	3900	1427	4541	786
	Polynomial 2	4027	1300	4622	705
	Polynomial 3	**4270**	**1057**	**4840**	**487**
	Polynomial 4	3775	1552	4450	877
	Polynomial 5	1322	4005	1522	3805
	Polynomial 6	1322	4005	1522	3805
	RBF	1725	3602	1869	3458
	Sigmoid	3831	1496	4353	974
MPL		3848	1479	4371	956

Concerning MPL, we employ many architectures while performing our experiments. However, we only present in this section the architectures of MPL associated with their corresponding parameters that generated the highest classification rates on VNEX data. Accordingly, classification rate of 72.24%, and 82.05% were accomplished, when 300 features were fed to the network (architecture I), in contrast to feeding an input features vector of length 400 (architecture II), respectively. Table 4 lists the details of both architectures.

It is worth mentioning that when hidden layers increase while employing MPL, the accuracy decreases. Consequently, providing the information of architecture II with the change of the numbers of hidden layers and the numbers of neurons per each layer, we have found that multiple hidden layers tend to reduce the accuracy of categorizing VNEX testing samples because of the overfitting. Fig. 10 depicts a graph for the change of the accomplished classification rate based on the change of the number of hidden layers.

Moreover, Fig. 11 illustrates a chart of classified versus misclassified samples of the VNEX dataset, where the total number of testing samples is 5, 327, input features

TABLE 4. Comparison between two architectures of MPL associated with their corresponding parameters and accuracy when extracting 300 features against 400 features of VNEX testing dataset.

MPL Architectures and parameters		Accuracy
Architecture I	Mean Square Error (MSE) = 0.009 Training iterations (epochs) = 17 Training rate = 0.0005 Error Threshold = 0.01 Max iteration = 500 Number of training samples = 5327 Number of testing samples = 5327 Input layer = 300 features vector Hidden layer = 1 Hidden neurons (in the hidden layer) = 1000 Output layer = 7 Activation function: sigmoid	72.24%
Architecture II	Mean Square Error (MSE) = 0.005 Training iterations (epochs) = 24 Training rate = 0.0005 Error Threshold = 0.01 Max iteration = 500 Number of training samples = 5327 Number of testing samples = 5327 Input layer = 400 features vector Hidden layer = 1 Hidden neurons (in the hidden layer) = 2000 Output layer = 7 Activation function: sigmoid	**82.05%**

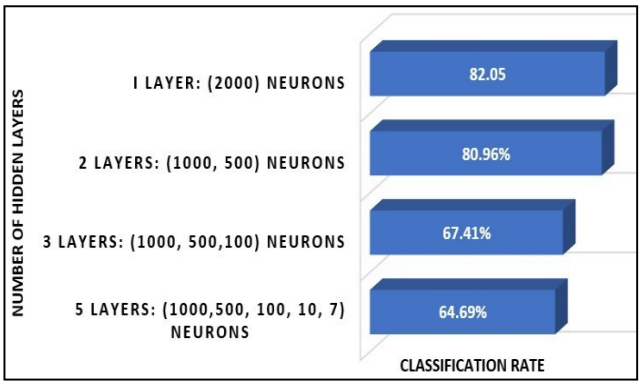

FIGURE 10. Graph illustrates the relationship between the classification rate and the number of hidden layers, where the input vector = 400, the output classes = 7, and using the testing set of VNEX dataset.

vector = 400, and the classification method is 1-against-1 multiclass SVM with degree 3 polynomial kernel. Out of 1522 for PDC samples, 966 for LF samples, 346 for LT samples, 394 for NC samples, 625 for WF samples, 980 for F samples, and 494 for SC samples, the number of misclassified samples were 58, 62, 65, 30, 105, 15, and 45, respectively. In this view, the lowest number of misclassified samples attained while categorizing F samples. In contrast, the highest number of misclassified samples obtained while classifying LT samples.

As seen in Table 5, the confusion matrix is also used to evaluate the performance of the multiclass SVM classifier

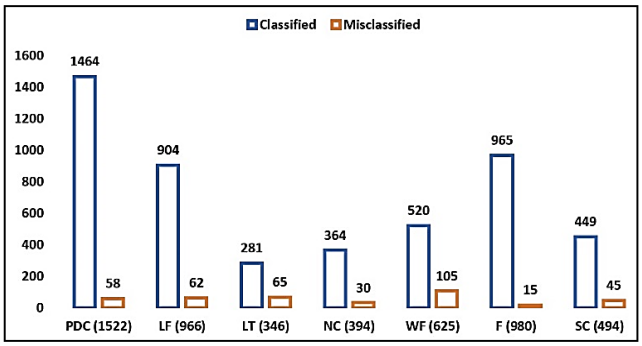

FIGURE 11. Graph of classified as opposed to misclassified images of VNEX testing set using the multiclass SVM with degree 3 polynomial kernel, and the input vector length = 400.

with degree 3 polynomial kernel on VNEX dataset, at which the testing set of 5, 327 samples were represented by 400 features, and the number of the output classes (labels) is equal to 7. It illustrates the correctly and incorrectly recognized samples for each class. The fact derived from the confusion matrix is that samples of the VNEX dataset are complex because of the similarity of regions among some still images of the phenomena under consideration. As a result, the average accuracy obtained was 90.85%. Precisely, the highest accuracy of 98.47% accomplished while testing fireworks samples with a few samples misclassified into LT and LF categories, because all three categories have a luminosity property. In contrast, the lowest accuracy of 81.21% achieved while testing LT samples with some samples misclassified into PDC, LF, WF, and F, as the nature of LT phenomena involves the existence of two regions including lava (luminous region) and tephra (non-luminous region) with varied density and color combinations of both regions in the scene during explosive or effusive eruptions. Likewise, WF achieved an accuracy of 83.2% with some of its samples misclassified into PDC, LF, LT, and F because of the presence of either visible flame region (luminous), smoke region (non-luminous) of white or gray to black colors of the smoke with different thickness, or both regions.

Consequently, evaluation results presented in the confusion matrix demonstrate that approximately a classification rate of 96.19%, 93.58%, 92.39%, and 90.89% were achieved for PDC, LF, NC, and SC, respectively. This indicates the effectiveness of the developed system. Nevertheless, the difficulty of the problem is obvious in the following cases. When a PDC phenomenon generated from a steam-driven, boiling-over, and continuous column collapse mechanisms, it may produce white dense clouds, which in turn will increase the possibility of incorrectly classifying some of PDC samples as if they belong to SC category. Also, some volcanoes may produce natural mushroom clouds under the gravity force, and thus those PDC samples may be incorrectly predicted by the classifier as NC. Similarly, sky clouds (SC) typically have a white color, some types form at low levels, and have different shapes such as vertical, heap, and fluffy resulting in misclassification for some SC samples

TABLE 5. The confusion matrix of multiclass SVM with degree 3 polynomial kernel.

Actual	Predicted results							Accuarcy
	PDC	LF	LT	NC	WF	F	SC	
PDC (1522)	**1464**	8	24	1	19	0	6	96.19%
LF (966)	28	**904**	8	1	15	10	0	93.58%
LT (346)	30	22	**281**	0	10	3	0	81.21%
NC (394)	14	5	8	**364**	3	0	0	92.39%
WF (625)	32	50	14	0	**520**	9	0	83.2%
F (980)	0	13	2	0	0	**965**	0	98.47%
SC (494)	43	0	0	0	2	0	**449**	90.89%

TABLE 6. Analysis of the execution time in milliseconds for testing one test sample.

Stage	Execution time
Extracting 100 texture features using PCA	15
Extracting 100 color features using YCbCr + PCA	19
Extracting 100 frequency features using Radix-2 FFT+ PCA	32
Extracting 100 histogram features using ULBP + PCA	21
Combining 400 features in an input vector	11
Passing 1 image to the classifier	1
Categorizing 1 image into a specific category	18
Total time in milliseconds	**117 ms**

as if they belong to PDC. Additionally, some SC samples were misclassified as if they belong to WF at which a dense white smoke appears in some observation during the smoldering stage of the combustion. Moreover, during the time frame of the growth of the nuclear mushroom cloud, a luminous fireball appears that results in misclassification of some samples as LF, LT, and WF. On the other hand, when the fireball is no longer luminous, some dense clouds were misclassified as PDC.

In addition, we examine the computational time required to categorize one test sample of VNEX dataset during the testing phase. To accomplish this goal, we split the total time frame into the following seven stages: (1) the time needed for computing 100 texture features using PCA, (2) the time consumed for extracting 100 color features using YCbCr + PCA, (3) the time consumed for extracting 100 frequency features using Radix-2 FFT + PCA, (4) the time consumed for extracting 100 histogram features using ULBP + PCA, (5) the time utilized to combine the measured 400 features in an input vector (6) the time needed to pass the test sample to the SVM, and (7) the categorization time utilized to predict the test sample label. Thus, the total execution time for classifying one test image was nearly 117ms. Table 6 provides the execution time related to each stage. As a result, we achieve a trade-off between the computation time and the accuracy while employing our proposed classification system.

Thus, if we processed every fourth frame of a 30fps video, our system can do a near real-time recognition of an explosion.

VIII. PROSPECTS FOR THE FUTURE

The proposed framework is pluggable and scalable. Thus, we discuss in this section the future trends for implementing advanced solutions to improve the classification rate in the context of the seven categories.

Our vision for future improvements involves applying different deep learning architectures to achieve supervised classification of the VNEX dataset. In this context, the autoencoder neural network can be employed. The Autoencoder is a nonlinear model that generalizes the PCA technique. It utilizes an adaptive, multilayer network called ''encoder'' in order to map the high dimensional data into a lower dimensional code. Furthermore, there is a similar ''decoder'' network that performs data recovery from the code [100]. Thus, the autoencoder sets the target values to be equal to the input values. During the learning phase, the autoencoder discovers weights to identify useful low-level features such as edges, primitive shapes, and more complex shapes. Then, the autoencoder combines them into a high feature space, and automatically learn the best nonlinear hyperplane that separate the input data into regions or categories.

Another alternative deep learning architecture that can be applied on the VNEX dataset called the Convolutional Neural Network (CNN). Recently, CNN has accomplished a remarkable performance in the computer vision field and has solved complex problems successfully [101]–[105]. Typically, the CNN comprises of numerous layers: (1) convolutional layers, (2) pooling layers, and (3) fully-connected layers. By fine-tuning the CNN architecture design, learning a representation of the discriminative features of the domain of our target application can be achieved automatically.

Furthermore, the Recurrent Neural Networks (RNN) using the Long Short-Term Memory (LSTM) architecture can be adopted to perform a supervised sequence learning on a dataset of videos for the respective seven classes. This model can be considered a convenient approach to monitor an explosion activity over time because of its capability on the prediction of time series, and context dependent pattern classification tasks [106], [107].

In an effort to improve the predictive accuracy of VNEX samples, the Decision Tree (DT) and the Random Forest (RF) algorithms can be applied. DT builds a classification model in the form of tree-structure. DT breaks down the dataset into smaller subsets while an associated decision is incrementally developed. Additionally, the RF algorithm is an ensemble of DT. RF is a combination of tree predictors in which each tree relies on the values of a random vector sampled independently and with the same distribution for all trees in the forest. The difference between the RF and the DT is that the process of finding the root node and splitting the feature nodes will run randomly using the RF algorithm. Moreover, RF helps to avoid the overfitting problem.

Today, our proposed classification system in the machine learning field can be further integrated with the latest research developments in the robotic field by using commercial drones that collect real-time video sequences from outdoor explosion zones, and send the captured frames to the client device via WiFi connection for testing. Powerful drones (Unmanned Aerial Vehicles) in terms of their ability to sustain in extreme weather conditions, are equipped with high resolution color cameras, have long connectivity range, and long battery life that can provide a good flight time are needed. Drones can access very dangerous locations where explosions occur, which are difficult for humans to explore. Once an active volcano has erupted, the area around the volcano's crater becomes hazardous for a few years and access is restricted to guarantee people's safety. Typically, video cameras are deployed permanently to monitor any volcanic eruptions. Once an eruption occurs, these cameras will be damaged, and the restricted area around the volcano will make it impossible to replace any of the video cameras. For example, in 1990, approximately all of the camera sensors malfunctioned during the eruption of Mt. Unzen-Fugen in Japan. Therefore, retrieving data about ash clouds was difficult. In this scenario, a drone would be a viable option to collect observations to be classified. In addition, drones are increasingly relied upon by military forces to observe a nuclear activity. In tactical situations, the drones monitor battlefields and thus, diminish the need for military personnel.

IX. CONCLUSION

We designed an efficient framework to categorize volcanic eruptions and nuclear explosions. Moreover, we collected a new dataset of color images referred to as VNEX. The totality of VNEX is 10, 654 samples that includes the following patterns: pyroclastic density currents, lava fountains, lava and tephra fallout, nuclear explosions, wildfires, fireworks, and sky clouds.

The proposed methodology incorporated various feature extraction approaches. Thus, we calculated the intensity levels to extract the texture features. Moreover, we utilized the YCbCr color model to calculate the amplitude features. We also employed the Radix-2 FFT to compute the frequency features. Furthermore, we used the ULBP technique to compute the histogram features. Moreover, we compute the PCA method on each feature class to calculate the most 100 significant eigenvectors and eigenvalues. These features were combined into a single input vector that provides valuable insight of the images, and fed into several classification techniques.

Through our experience and experiments, we determined that VNEX samples are complex. Nevertheless, the 1-against-1 multiclass SVM with degree 3 polynomial kernel produced the highest classification rate of 90.85% when employed on 5, 327 samples of VNEX testing set, and the total execution time of approximately 117ms was consumed to classify one

test sample. Thus, a trade-off between the computation time and the accuracy was achieved.

REFERENCES

[1] S. Abusaleh, A. Mahmood, K. Elleithy, and S. Patel, "A novel vision-based classification system for explosion phenomena," *J. Imag.*, vol. 3, no. 2, p. 14, Apr. 2017, doi: 10.3390/jimaging3020014.

[2] J. Gyakum and J. Stix. (Jan./Apr. 2015). Natural disasters. McGill University, Montreal, QC, Canada. Accessed: Oct. 1, 2017. [Online] Available: https://courses.edx.org

[3] B. W. Pipkin, D. D. Trent, R. Hazlett, and P. Bierman, *Geology and the Environment*, 6th ed., Belmont, CA, USA: Brooks/Cole, 2010.

[4] R. Tilling, C. Heliker, and D. Swanson, *Eruptions of Hawaiian Volcanoes—Past, Present, and Future* (General Information Product 117), 2nd ed. Reston, VA, USA: U.S. Department of the Interior, U.S. Geological Survey, 2010.

[5] R. Lopes, *The Volcano Adventure Guide*. Cambridge, U.K.: Cambridge Univ. Press, 2005.

[6] F. R. Spellman, *Geography for Nongeographers*. New York, NY, USA: Scarecrow, 2010.

[7] R. Wicander and J. S. Monroe, *Essentials of Physical Geology*, 5th ed. Belmont, CA, USA, Brooks/Cole, 2009.

[8] P. P. Craig and J. A. Jungerman, *Nuclear Arms Race: Technology and Society*. 2nd ed. New York, NY, USA: McGraw-Hill, 1990.

[9] S. C. Moran *et al.*, "Instrumentation recommendations for volcano monitoring at U.S. volcanoes under the national volcano early warning system," Dept. Interior, U.S. Geol. Survey, Reston, VA, USA, Sci. Invest. Rep. 2008-5114, 2008.

[10] U.S. Department of the Interior, U.S. Geological Survey, and Volcano Hazards Program. (Jan. 7, 2016). *Temperatures at the Surface Reflect Temperatures Below the Ground*. Accessed: Oct. 1, 2017. [Online]. Available: https://volcanoes.usgs.gov/vhp/thermal.html

[11] F. S. Marzano, M. Lamantea, M. Montopoli, S. Di Fabio, and E. Picciotti, "The Eyjafjöll explosive volcanic eruption from a microwave weather radar perspective," *Atmos. Chem. Phys.*, vol. 11, no. 18, pp. 9503–9518, 2011.

[12] U.S. Department of the Interior, U.S. Geological Survey, and Volcano Hazards Program. (May 30, 2017). *Using Digital Elevation Models (DEMs) to Map Changes in Topography*. Accessed on: Oct. 1, 2017. [Online]. Available: https://volcanoes.usgs.gov/volcanoes/st_helens/st_helens_monitoring_109.html

[13] L. Wang and M. J. Alexander, "Global estimates of gravity wave parameters from GPS radio occultation temperature data," *J. Geophys. Res.*, vol. 115, p. D21122, Nov. 2010, doi: 10.1029/2010JD013860.

[14] M. Blackett, "An overview of infrared remote sensing of volcanic activity," *J. Imag.*, vol. 3, no. 2, p. 13, Apr. 2017, doi: 10.3390/jimaging3020013.

[15] H. Dickinson and P. Tamarkin, "Systems for the detection and identification of nuclear explosions in the atmosphere and in space," *Proc. IEEE*, vol. 53, no. 12, pp. 1921–1934, Dec. 1965, doi: 10.1109/PROC.1965.4469.

[16] S. Self, "The effects and consequences of very large explosive volcanic eruptions," *Philos. Trans. Roy. Soc. London A, Math. Phys. Sci.*, vol. 364, no. 1845, pp. 2073–2097, 2006, doi: 10.1098/rsta.2006.1814.

[17] M. J. Branney and P. Kokelaar, *Pyroclastic Density Currents and the Sedimentation of Ignimbrites*. London, U.K.: Geological Society of London, 2002.

[18] T. Shea, L. Gurioli, B. F. Houghton, R. Cioni, and K. V. Cashman, "Column collapse and generation of pyroclastic density currents during the A.D. 79 eruption of Vesuvius: The role of pyroclast density," *Geology*, vol. 39, no. 7, pp. 695–698, Jul. 2011, doi: 10.1130/G32092.1.

[19] R. Sulpizio, P. Dellino, D. M. Doronzo, and D. Sarocchi, "Pyroclastic density currents: State of the art and perspectives," *J. Volcanol. Geothermal Res.*, vol. 283, pp. 36–65, Aug. 2014, doi: 10.1016/j.jvolgeores.2014.06.014.

[20] G. E. Bogoyavlenskaya, O. A. Braitseva, I. V. Melekestsev, V. Y. Kiriyanov, and C. D. Miller, "Catastrophic eruptions of the directed-blast type at Mount St. Helens, bezymianny and Shiveluch volcanoes," *J. Geodyn.*, vol. 3, pp. 189–218, Oct. 1985.

[21] I. A. Nairn and S. Self, "Explosive eruptions and pyroclastic avalanches from Ngauruhoe in February 1975," *J. Volcanol. Geothermal Res.*, vol. 3, pp. 39–60, Mar. 1978.

[22] Smithsonian Institution. *National Museum of Natural History, Global Volcanism Program, Types and Processes Gallery*. Accessed: Oct. 1, 2017. [Online]. Available: http://volcano.si.edu/learn_galleries.cfm?p=9

[23] N. Lardot. (Oct. 2006). Pyroclastic Flows at Mayon Volcano.JPG. U.S Department of the Interior, U.S. Geological Survey. Accessed: Oct. 1, 2017. [Online]. Available: https://commons.wikimedia.org/wiki/File:Pyroclastic_flows_at_Mayon_Volcano.jpg

[24] B. Voight. Soufriere Hills Volcano Erupting. National Science Foundation (NSF). Accessed: Aug. 20, 2017. [Online]. Available: https://www.nsf.gov/news/mmg/mmg_disp.jsp?med_id=64852&from=img

[25] T. Pfeiffer. (Sep. 17, 2004). Volcano Discovery. Bromo Volcano (Tengger Caldera), Indonesia. Accessed: Oct. 1, 2017. [Online]. Available: http://www.decadevolcano.net/volcanoes/indonesia/tengger_caldera/bromo.html

[26] U.S. Department of the Interior, U.S. Geological Survey, and Volcano Hazards Program. (Jul. 28, 2015). Glossary-Eruption Column. Accessed: Oct. 1, 2017. [Online]. Available: http://volcanoes.usgs.gov/vsc/glossary/eruption_column.html

[27] Volcanic Ashfall Impacts Working Group, U.S Department of the Interior, and U.S. Geological Survey. (Dec. 17, 2015). Volcanic Ash Impacts and Mitigation—Mt St Helens 1980. Accessed: Oct. 1, 2017. [Online]. Available: https://volcanoes.usgs.gov/volcanic_ash/mount_st_helens_1980.html

[28] (Mar. 19, 2009). *TVNZ One News-Undersea Volcano Eruption 09 [Tonga]*. Accessed: Oct. 1, 2017. [Online]. Available: https://www.youtube.com/watch?v=B1tjIihHgco

[29] U.S. Department of the Interior, U.S. Geological Survey, and Volcano Hazards Program. (Jul. 10, 2015). *Glossary-Effusive Eruption*. Accessed: Oct. 1, 2017, [Online]. Available: https://volcanoes.usgs.gov/vsc/glossary/effusive_eruption.html

[30] U.S. Department of the Interior, U.S. Geological Survey, Volcano Hazards Program, and Hawaiian Volcano Observatory (HVO). (May 30, 2017). *A Recap of the Kamoamoa Fissure Eruption on its Third Anniversary*. Accessed: Oct. 1, 2017. [Online]. Available: https://volcanoes.usgs.gov/observatories/hvo/hvo_volcano_watch.html?vwid=218

[31] U.S. Department of the Interior, U.S. Geological Survey, Volcano Hazards Program, and Hawaiian Volcano Observatory. (May 7, 2017). *Pu'u 'Ō'ō and the Current Eruption of Kīlauea*. Accessed: Oct. 1, 2017. [Online]. Available: https://volcanoes.usgs.gov/volcanoes/kilauea/geo_hist_1983.html

[32] J. Seach. *Volcano Live, Lava Colour | John Seach*. Accessed: Oct. 1, 2017. [Online]. Available: http://www.volcanolive.com/lava2.html

[33] D. Karnå. (Jun. 2, 2010). *Eyjafjallajökull Major Eruption 20100510.JPG*. Accessed: Oct. 1, 2017. [Online]. Available: https://commons.wikimedia.org/wiki/File:Eyjafjallaj%C3%B6kull_major_eruption_20100510.jpg

[34] T. Pfeiffer. (Jan. 31, 2004). *Volcano Discovery. ETNA Volcano Photos*. Accessed: Oct. 1, 2017. [Online]. Available: http://www.decadevolcano.net/photos/etna1002_2.htm

[35] How Volcanoes Work. *Tephra and Pyroclastic Rocks*. Accessed: Oct. 1, 2017. [Online]. Available: http://www.geology.sdsu.edu/how_volcanoes_work/Tephra.html

[36] Trinity Atomic Web Site. *Gallery of Test Photos, 1995–2003*, Accessed: Oct. 1, 2017. [Online]. Available: http://www.abomb1.org/testpix/index.html

[37] M. Jinguuji and S. Ehara, "Quantitative estimation of erupted volcanic ash by using satellite image," In *Proc. IEEE Int. Geosci. Remote Sens. Symp. (IGARSS)*, Jul. 1998, pp. 1345–1347, doi: 10.1109/IGARSS.1998.691405.

[38] *Monitoring Earth's Subsurface From Space*. Lawrence Livermore Nat. Lab., Livermore, CA, USA, Apr. 2005, pp. 4–11.

[39] B. Andò and E. Pecora, "A measurement tool for investigating the volcanic activity," in *Proc. IEEE Instrum. Meas. Technol. Conf.*, May 2005, pp. 2039–2043, doi: 10.1109/IMTC.2005.1604532.

[40] H. Langer, S. Falsaperla, M. Masotti, R. Campanini, S. Spampinato, and A. Messina, "Synopsis of supervised and unsupervised pattern classification techniques applied to volcanic tremor data at Mt Etna, Italy," *Geophys. J. Int.*, vol. 178, no. 2, pp. 1132–1144, Aug. 2009, doi: 10.1111/j.1365-246X.2009.04179.x.

[41] A. S. Iyer, F. M. Ham, and M. A. Garces, "Neural classification of infrasonic signals associated with hazardous volcanic eruptions," in *Proc. IEEE Int. Joint Conf. Neural Netw.*, San Jose, CA, USA, Jul./Aug. 2011, pp. 336–341, doi: 10.1109/IJCNN.2011.6033240.

[42] M. Picchiani *et al.*, "Volcanic ash detection and retrievals using MODIS data by means of neural networks," *Atmos. Meas. Tech.*, vol. 4, pp. 2619–2631, Dec. 2011, doi: 10.5194/amt-4-2619-2011.

[43] B. Payette. (Sep. 2002). *Color Space Convertor: R'G'B' to Y'CbCr, Xilinx, XAPP637 (v1.0)*. Accessed: Oct. 1, 2017. [Online]. Available: http://application-notes.digchip.com/077/77-42796.pdf

[44] K. Jack, *Video Demystified: A Handbook for the Digital Engineer*, 3rd ed. Eagle Rock, VA, USA: LLH Technology Publishing, 2001.

[45] [45] S.W. Smith, "The fast fourier transform," in *The Scientist and Engineer's Guide to Digital Signal Processing*, San Diego, CA, USA, ch. 12. Accessed: Oct. 1, 2017, [Online]. Available: http://www.dspguide.com/ch12.htm

[46] S. Rapuano and F. J. Harris, "An introduction to FFT and time domain windows," *IEEE Instrum. Meas. Mag.*, vol. 10, no. 6, pp. 32–44, Dec. 2007, doi: 10.1109/MIM.2007.4428580.

[47] D. Huang, C. Shan, M. Ardabilian, Y. Wang, and L. Chen, "Local binary patterns and its application to facial image analysis: A survey," *IEEE Trans. Syst., Man, Cybern. C, Appl. Rev.*, vol. 41, no. 6, pp. 765–781, Nov. 2011, doi: 10.1109/TSMCC.2011.2118750.

[48] L. Ali, T. Kasetkasem, F. G. Khan, T. Chanwimaluang, and H. Nakahara, "Identification of inpainted satellite images using evalutionary artificial neural network (EANN) and k-nearest neighbor (KNN) algorithm," in *Proc. 8th Int. Conf. Inf. Commun. Technol. Embedded Syst. (IC-ICTES)*, May 2017, pp. 1–6, doi: 10.1109/ICTEmSys.2017.7958765.

[49] C. J. C. Burges, "A tutorial on support vector machines for pattern recognition," *Data Mining Knowl. Discovery*, vol. 2, no. 2, pp. 121–167, 1998.

[50] C. W. Hsu, C. C. Chang, and C. J. Lin. (2010). *A Practical Guide to Support Vector Classification*. Accessed: Oct. 1, 2017. [Online]. Available: http://www.csie.ntu.edu.tw/~cjlin/papers/guide/guide.pdf

[51] J. C. Platt, "Fast training of support vector machines using sequential minimal optimization," in *Advances in Kernel Methods-Support Vector Learning*, B. Scholkopf, C. J. C. Burges, and A. J. Smola, Eds. Cambridge, MA, USA: MIT Press, 1998.

[52] R. C. Gonzalez and R. E. Woods, *Digital Image Processing*, 3rd ed. Upper Saddle River, NJ, USA: Prentice-Hall, 2008.

[53] *U.S. Geological Survey*. Accessed: Oct. 1, 2017. [Online]. Available: https://www.usgs.gov/

[54] *Wikimedia Commons*. Accessed: Oct. 1, 2017. [Online]. Available: https://commons.wikimedia.org/wiki/Main_Page

[55] T. Pfeiffer. *Volcano Adventures*. Accessed: Oct. 1, 2017. [Online]. Available: https://www.volcano-adventures.com/es/about_us.html

[56] T. Pfeiffer. *Volcano Discovery*. Accessed: Oct. 1, 2017. [Online]. Available: http://www.decadevolcano.net/index.htm

[57] Department of Commerce, National Oceanic and Atmospheric Administration, and National Weather Service. *Clouds-Introduction to Clouds*. Accessed: Oct. 1, 2017. [Online]. Available: http://www.weather.gov/

[58] *PEXELS Blog*. Accessed: Oct. 1, 2017. [Online]. Available: https://www.pexels.com/

[59] U.S. Environmental Protection Agency, U.S. Forest Service, U.S. Centers for Disease Control and Prevention, and California Air Resources Board. (May 2016). *Wildfire Smoke—A Guide for Public Health Officials*. Accessed: Oct. 1, 2017. [Online]. Available: https://www3.epa.gov/airnow/wildfire_may2016.pdf

[60] B. J. Alan Company. *Fireworks University—Fireworks Glossary*. Accessed: Oct. 1, 2017. [Online]. Available: http://www.fireworks.com/fireworks-university/fireworks-glossary/

[61] The Fireworks Alliance. *Glossary of Fireworks Terms, Powered by Accelix*. Accessed: Oct. 1, 2017. [Online]. Available: http://www.fireworksalliance.org/cgi-bin/viewpage.pl?p=glossary#w

[62] J. A. Conkling and C. J. Mocella, *Chemistry of Pyrotechnics: Basic Principles and Theory*, 2nd ed. New York, NY, USA: CRC Press, 2010.

[63] National Aeronautics and Space Administration (NASA). *S'COOL Cloud Identification Chart, EW-2004-10-04-LaRC*. Accessed: Oct. 1, 2017. [Online]. Available: http://science-edu.larc.nasa.gov/SCOOL/pdf/Cloud_ID.pdf

[64] National Weather Service, National Oceanic and Atmospheric Administration, and Department of Commerce. (Mar. 14, 2013). *Ten Basic Cloud Types*. Accessed: Oct. 1, 2017. [Online]. Available: http://www.srh.noaa.gov/srh/jetstream/clouds/cloudwise/types.html

[65] U.S. Department of the Interior, U.S. Geological Survey, and Volcano Hazards Program. (Aug. 21, 2015). *Explosive Eruption*. Accessed: Oct. 1, 2017. [Online]. Available: https://volcanoes.usgs.gov/vsc/glossary/explosive_eruption.html

[66] U.S. Department of the Interior, U.S. Geological Survey, and Volcano Hazards Program. (Feb. 12, 2016). *Pyroclastic Flows Move Fast and Destroy Everything in Their Path*. Accessed: Oct. 1, 2017. [Online]. Available: https://volcanoes.usgs.gov/vhp/pyroclastic_flows.html

[67] U.S. Department of the Interior, U.S. Geological Survey, and Volcano Hazards Program. (May 10, 2017). *Explosive Eruptions Produce Multiple Hazards*. Accessed: Oct. 1, 2017. [Online]. Available: https://volcanoes.usgs.gov/observatories/hvo/hawaii_explosive_eruptions.html

[68] R. Clucas, U.S. Department of the Interior, and U.S. Geological Survey. (Apr. 21, 1990). *Volcanoes of the Wrangell Mountains and Cook Inlet Region, Alaska-Selected Photographs-Album*. Accessed: Oct. 1, 2017. [Online]. Available: http://web.archive.org/web/20051111095409/http://wrgis.wr.usgs.gov/dds/dds-39/album.html

[69] A. Sauter. (Aug. 26, 2010). *Ocean Explorer, U.S. Office of Ocean Exploration and Research, National Oceanic and Atmospheric Administration, U.S. Department of Commerce*. Accessed: Oct. 1, 2017. [Online]. Available: http://oceanexplorer.noaa.gov/explorations/03fire/logs/anatahan/media/fig1.html

[70] ITU, Wikimedia Commons. (Apr. 25, 2015). *File: Calbuco (17071015700).JPG*. Accessed: Oct. 1, 2017. [Online]. Available: https://commons.wikimedia.org/wiki/File:Calbuco_(17071015700).jpg

[71] Paginario. (Sep. 21, 2009). *Wikimedia Commons, File: Erupcion Guagua RGB.JPG*. Accessed: Oct. 1, 2017. [Online]. Available: https://commons.wikimedia.org/wiki/File:Erupcion_guagua_rgb.jpg

[72] R. Russell. (Dec. 2, 2016). Alaska Volcano Observatory, U.S. Geological Survey, IMAGE 428. Accessed: Oct. 1, 2017. [Online]. Available: https://avo.alaska.edu/images/image.php?id=428

[73] J. B. Judd. (May 1, 1997). *USGS*. Accessed: Oct. 1, 2017. [Online]. Available: https://pubs.usgs.gov/gip/hawaii/page29.html

[74] U.S. Department of the Interior, U.S. Geological Survey, and Volcano Hazards Program. (Apr. 13, 2017). *1959 Kīlauea IKI Eruption*. Accessed: Oct. 1, 2017. [Online]. Available: https://volcanoes.usgs.gov/volcanoes/kilauea/geo_hist_kilauea_iki.html

[75] G. E. Sigvaldason. (May 5, 1999). USGS—Lava Fountains, Nordic Volcanological Institute, Reykjavik, Iceland. Accessed: Oct. 1, 2017. [Online]. Available: https://pubs.usgs.gov/gip/dynamic/Krafla.html

[76] T. Pfeiffer. *Volcano Discovery, Erta Ale Volcano Nov 2010: Lava Fountains*. Accessed: Oct. 1, 2017. [Online]. Available: https://www.volcanodiscovery.com/photos/erta-ale/nov10/lava-fountains.html

[77] T. Pfeiffer. *Volcano Discovery, Stromboli Trekking*. Accessed: Oct. 1, 2017. [Online]. Available: https://www.volcanodiscovery.com/stromboli/climbing/tour.html

[78] T. Pfeiffer. *Volcano Discovery, Kilauea Volcano Special*. Accessed: Oct. 1, 2017. [Online]. Available: https://www.volcanodiscovery.com/es/hawaii/kilauea_volcano_special.html

[79] T. Pfeiffer. *Volcano Discovery, Photos of Volcanoes-Bárdarbunga*. Accessed: Oct. 1, 2017. [Online]. Available: https://www.volcanodiscovery.com/photos/volcanoes.html

[80] T. Pfeiffer. *Volcano Discovery, Etna Volcano Photos. Part I*. Accessed: Oct. 1, 2017. [Online]. Available: http://www.decadevolcano.net/photos/etna0701_1.html

[81] T. Pfeiffer. *Volcano Discovery, Etna Volcano Photos. Part 1*. Accessed: Oct. 1, 2017. [Online]. Available: http://www.decadevolcano.net/photos/etna1002_1.html

[82] T. Pfeiffer. *Volcano Discovery, Etna Volcano Photos. Part 3*. Accessed: Oct. 1, 2017. [Online]. Available: http://www.decadevolcano.net/photos/etna1002_3.html

[83] T. Pfeiffer. *Volcano Discovery, Etna Volcano Photos. Part 2*. Accessed: Oct. 1, 2017. [Online]. Available: http://www.decadevolcano.net/photos/etna1002_2.html

[84] The National Security Archive, The George Washington University. (2017). *The Atomic Tests at Bikini Atoll, July 1946*. Accessed: Oct. 1, 2017. [Online]. Available: http://nsarchive2.gwu.edu/nukevault/ebb553-70th-anniversary-of-Crossroads-atomic-tests/

[85] J. Newman. (Oct. 17, 2007). *Wikimedia Commons, File:Zaca3.JPG*. Accessed: Oct. 1, 2017. [Online]. Available: https://commons.wikimedia.org/wiki/File:Zaca3.jpg

[86] T. Bulyonkova. (Aug. 19, 2013). *Wikimedia Commons, File:Yugansky Nature Reserve Fire (7938021666).JPG*. Accessed: Oct. 1, 2017. [Online]. Available: https://commons.wikimedia.org/wiki/File:Yugansky_nature_reserve_fire_(7938021666).jpg
[87] Tilo. (Aug. 1, 2005). *Wikimedia Commons, File: Waldbrand-Bodenfeuer.JPG*. Accessed: Oct. 1, 2017. [Online]. Available: https://commons.wikimedia.org/wiki/File:Waldbrand-Bodenfeuer.jpg
[88] E. Saltine. (Oct. 30, 2003). *Wikimedia Commons, File: Wildfire.JPG*. Accessed: Oct. 1, 2017. [Online]. Available: https://commons.wikimedia.org/wiki/File:Wildfire.jpg
[89] R. Keith. (Mar. 1, 2013). *Wikimedia Commons, File: A Large Fire in Tropical Forest Trees in the Fire.JPG*. Accessed: Oct. 1, 2017. [Online]. Available: https://commons.wikimedia.org/wiki/File:A_large_fire_in_tropical_forest_trees_in_the_fire.jpg
[90] G. Vicker. (Mar. 1, 2013). *Wikimedia Commons, File: Big Fire Burning Big Fire Flames.JPG, U.S. Fish and Wildlife Service*. Accessed: Oct. 1, 2017. [Online]. Available: https://commons.wikimedia.org/wiki/File:Big_fire_burning_big_fire_flames.jpg
[91] F. Schulke. *Wikimedia Commons, File: Forest Fire in the Everglades, Collier County. Fires are Fairly Common in the Everglades in dry Seasons or dry Years—NARA-548591.JPG, U.S. National Archives and Records Administration*. Accessed: Oct. 1, 2017. [Online]. Available: https://commons.wikimedia.org/wiki/File:FOREST_FIRE_IN_THE_EVERGLADES,_COLLIER_COUNTY._FIRES_ARE_FAIRLY_COMMON_IN_THE_EVERGLADES_IN_DRY_SEASONS_OR_DRY_YEARS._-_NARA_-_548591.jpg
[92] US Air Force. (Aug. 4, 2014). *Wikimedia Commons, File: High Park Fire.JPG*. Accessed: Oct. 1, 2017. [Online]. Available: https://commons.wikimedia.org/wiki/File:High_Park_fire.jpg
[93] T. Bulyonkova. (Aug. 19, 2013). *Wikimedia Commons, File: Yugansky Nature Reserve Fire (7938012202).JPG*. Accessed: Oct. 1, 2017. [Online]. Available: https://commons.wikimedia.org/wiki/File:Yugansky_nature_reserve_fire_(7938012202).jpg
[94] S. Eugster. (Apr. 7, 2005). *Wikimedia Commons, File: Cirrocumulus to Altocumulus.JPG*. Accessed: Oct. 1, 2017. [Online]. Available: https://commons.wikimedia.org/wiki/File:Cirrocumulus_to_Altocumulus.JPG
[95] Saperaud. (Sep. 3, 2004). *Wikimedia Commons, File: Sc2.JPG*. Accessed: Oct. 1, 2017. [Online]. Available: https://commons.wikimedia.org/wiki/File:Sc_2.jpg
[96] S. Eugster. (Sep. 10, 2015). *Wikimedia Commons, File: Big Cumulonimbus.JPG*. Accessed: Oct. 1, 2017. [Online]. Available: https://commons.wikimedia.org/wiki/File:Big_Cumulonimbus.JPG
[97] Joniprittie. (Dec. 15, 2009). *Wikimedia Commons, File: Brightbluesky.JPG*. Accessed: Oct. 1, 2017. [Online]. Available: https://commons.wikimedia.org/wiki/File:Brightbluesky.jpg
[98] M. Jastremski. (Jul. 10, 2005). *Wikimedia Commons, File: Cumulus Clouds in Fair Weather.JPEG*. Accessed: Oct. 1, 2017. [Online]. Available: https://commons.wikimedia.org/wiki/File:Cumulus_clouds_in_fair_weather.jpeg
[99] L. Diosan, M. Oltean, A. Rogozan, and J. P. Pecuchet, "Genetically designed multiple-kernels for improving the SVM performance," *Proc. 9th Annu. Conf. Genetic Evol. Comput. (GECCO)*, London, U.K., Jul. 2007, p. 1873.
[100] A. Ng, "CS294A lecture notes—Sparse autoencoder," Stanford Univ., Stanford, CA, USA, Tech. Rep., 2011, pp. 1–19, accessed: Oct. 1, 2017. [Online]. Available: https://web.stanford.edu/class/cs294a/sparseAutoencoder_2011new.pdf
[101] A. Esteva *et al.*, "Dermatologist-level classification of skin cancer with deep neural networks," *Nature*, vol. 542, pp. 115–118, Feb. 2017, doi: 10.1038/nature21056.
[102] A. Krizhevsky, I. Sutskever, and G. E. Hinton, "ImageNet classification with deep convolutional neural networks," in *Proc. Adv. Neural Inf. Process. Syst.*, vol. 1. 2012, pp. 1106–1114.
[103] Y. Liu *et al.*. (May 2016). "Application of deep convolutional neural networks for detecting extreme weather in climate datasets." [Online]. Available: [Online]. Available: https://arxiv.org/abs/1605.01156
[104] A. Conneau, H. Schwenk, L. Barrault, and Y. LeCun. (Jun. 2016). "Very deep convolutional networks for text classification." [Online]. Available: https://arxiv.org/abs/1606.01781
[105] C. Farabet, C. Couprie, L. Najman, and Y. LeCun, "Learning hierarchical features for scene labeling," *IEEE Trans. Pattern Anal. Mach. Intell.*, vol. 35, no. 8, pp. 1915–1929, Aug. 2013 doi: 10.1109/TPAMI.2012.231.
[106] A. Graves, A. Mohamed, and G. Hinton, "Speech recognition with deep recurrent neural networks," in *Proc. IEEE Int. Conf. Acoust., Speech Signal Process.*, May 2013, pp. 6645–6649, doi: 10.1109/ICASSP.2013.6638947.
[107] A. Karpathy, J. Johnson, and L. Fei-Fei. (Jun. 2015). "Visualizing and understanding recurrent networks." [Online]. Available: https://arxiv.org/abs/1506.02078

SUMAYA ABUSALEH (M'13) received the Associate's degree in programming from Ma'an College, Al-Balqa Applied University, Jordan, in 2000, the B.S. degree in computer science from Mu'tah University, Jordan, in 2003, and the M.S. degree in computer science from Amman Arab University, Jordan, in 2007. She is currently pursuing the Ph.D. degree with the Computer Science and Engineering Department, University of Bridgeport (UB), Bridgeport, CT, USA.

She is currently a Research Associate with the School of Engineering, UB. From 2013 to 2016, she was a Graduate Assistant with the School of Engineering, UB. From 2005 to 2009, she was a Lecturer with the Information Technology Department, Al-Balqa Applied University, Ma'an College, Jordan, and where she was a System Administrator from 2003 to 2005.

Miss Abusaleh has research interests in the areas of computer vision, deep learning, robotics, wireless sensor networks, and network security. She served as a Student Member of the Technical Program Committee of the International Joint Conference on Computer, International, and System Science, and Engineering organized by the School of Engineering, UB, from 2010 to 2013. She also served as a Reviewer for the IEEE Access journal in 2018.

Miss Abusaleh is a Student Member of the IEEE Young Professionals, the IEEE WIE, the ACM, and the SWE organizations. She received the Scholar Citizen Award in the Annual Student Leadership Recognition Banquet, UB, in 2013. She has also been recognized by the Honor Society of Upsilon Pi Epsilon Organization in 2013.

AUSIF MAHMOOD (SM'82) received the M.S. and Ph.D. degrees in electrical and computer engineering from Washington State University, USA. He is currently the Chair Person of the Computer Science and Engineering Department and a Professor with the Computer Science and Engineering Department and the Electrical Engineering Department, University of Bridgeport, Bridgeport, CT, USA. His research interests include parallel and distributed computing, computer vision, deep learning, and computer architecture.

KHALED M. ELLEITHY (SM'13) received the B.Sc. degree in computer science and automatic control and the M.S. degree in computer networks from Alexandria University in 1983 and 1986, respectively, and the M.S. and Ph.D. degrees in computer science from the Center for Advanced Computer Studies, University of Louisiana at Lafayette, in 1988 and 1990, respectively. He is currently an Associate Vice President for graduate studies and research at the University of Bridgeport, and a Professor of computer science and engineering.

He has authored over 400 research papers in national/international journals and conferences in his areas of expertise. He is an editor or co-editor for 12 books published by Springer. His research interests include wireless sensor networks, mobile communications, network security, quantum computing, and formal approaches for design and verification. He supervised hundreds of senior projects, M.S. theses, and Ph.D. dissertations. He developed and introduced many new undergraduate/graduate courses. He also developed new teaching/research laboratories in his area of expertise.

Dr. Elleithy was a recipient of the Connecticut Quality Improvement Award Gold Innovation Prize, CT, USA, in 2015. He was a recipient of the Distinguished Professor of the Year at the University of Bridgeport from 2006 to 2007. His students received over twenty prestigious national/international awards from the IEEE, the ACM, and the ASEE.

Dr. Elleithy is a member of the technical program committees of many international conferences as recognition of his research qualifications. He is also a member of several technical and honorary societies. He is a Senior Member of the IEEE Computer Society. He has been a member of the ACM since 1990, a member of the ACM Special Interest Group on Computer Architecture since 1990, a member of the Honor Society of Phi Kappa Phi University of South Western Louisiana Chapter since 1989, a member of the IEEE Circuits and Systems society since 1988, a member of the IEEE Computer Society since 1988, and a Lifetime Member of the Egyptian Engineering Syndicate since 1983. He was the Chair Person of the International Conference on Industrial Electronics, Technology, and Automation in 2001, and the Chair Person of the Connecticut Conference on Industrial Electronics, Technology, and Automation in 2016. He is the Co-Chair and the Co-Founder of the Annual International Joint Conferences on Computer, Information, and Systems Sciences, and Engineering Virtual Conferences from 2005 to 2014. He served as a guest editor for several international journals.